FEATURE ARTICLE

Controlled Colloidal Assembly: Experimental Modeling of General Crystallization and Biomimicking of Structural Color

*Ying Ying Diao and Xiang Yang Liu**

This paper aims to give an overview on the recent progress of controlled colloidal assembly as a unique experimental modeling system to study the general crystallization mechanism, i.e., the kinetics of nucleation, growth, and defects formation, and as a template for photonic crystals engineering. Such a system allows us not only to visualize some "atomic" details of the nucleation and surface process of crystallization, but also to treat quantitatively the previous models to an extent that has never been achieved before by other approaches. As such, the kinetic process of nucleation was quantitatively examined at the single particle level for the first time, allowing the identification of the deviations from the classical theories. The application of the electrically controlled colloidal crystallization to the modeling of the kinetics of some important processes of crystallization, i.e., multistep crystallization, supersaturation-driven structural mismatch nucleation, defect creation and migration kinetics, surface roughening, etc., has brought our knowledge to a new phase. Apart from the fundamental aspects, the controlled colloidal crystallization has attracted significant attention in many applications. In this regard, the application of colloidal crystallization to the fabrication of photonic crystals and the biomimicking of natural structure colors will be examined.

1. Introduction

Colloids are dispersions of nano/microsized particles in a fluid background solvent. Common examples range from ink, milk, mayonnaise, paint, and smoke, so their study has a myriad of practical applications.[1–3] In terms of applications, there is great interest in controlling the colloidal assembly, which could be employed to define a template for creating two-dimensional (2D)/three-dimensional (3D) periodic structures for applications in photonic devices,[4,5] biological and chemical sensors,[6] and tunable lasers.[7] Apart from the applications, colloids have been employed as a model system to study phase transitions.[8–13] In this regard, these nano/micronsized colloids provide an important platform for sampling the aggregation and assembly at the single-particle level because of its visible size, slow dynamics, and tunable interparticle interactions.[1–3,14–18] In addition, colloidal particles in solutions behave like big "atoms"[10,11] and the phase behavior of colloidal suspensions is similar to that of atomic and molecular systems.[12] The advantage of this model system is that the growth units are colloidal particles, and thus the crystallization process can be observed directly by a normal optical microscope. Furthermore, the interaction between colloidal particles can be turned by the adjustment of the ionic strength, pH of solutions/suspensions, and the applied field strength and frequency, etc. Therefore the thermodynamic driving force for the crystallization can be controlled precisely in a colloidal system. In this sense, the quantitative measurement and the data interpretation become possible.[11,12] Moreover, proteins and viruses are in the colloidal domain. Any advantage in the understanding of colloidal crystallization will exert a direct impact on the control of proteins and other biomacromolecules crystallization.

We notice that crystallization plays a crucial role in the preparation of functional materials,[19–22] the structural characterization of natural and synthetic molecules,[23,24] and the development of advanced technologies.[25,26] Many nano materials are crystalline phases and the essential structures and most important properties of the systems are determined by nucleation and the correlation between the nucleating nano phase and the substrate, etc. Nowadays, the control of nano crystallization is directly related to some soft materials and nanophase formation.[27] From the technological point of view, the knowledge of nucleation, growth, and defect generation is very important in identifying robust technologies in electronic, photonic and life science technologies.

Up to now, crystallization was still considered as art rather than science, mainly because there is not sufficient knowledge on its critical early stages and the atomic processes. In this regard, the kinetics of the transition from the metastable structure to the stable structure has so far been open to question. The key challenge is the in situ imaging of the atomic/molecular dynamic process, which is limited by both the spatial and the temporal definition of current technologies and the absence of the direct observation on the transition process in real-space, except for some local events of crystallization/

Y. Y. Diao, Prof. X. Y. Liu
Department of Physics and Department of Chemistry
National University of Singapore
2 Science Drive 3, Singapore 117542
E-mail: phyliuxy@nus.edu.sg

DOI: 10.1002/adfm.201102288

quasi-crystallization of large species, namely proteins[28] and colloidal particles.[29] Notice that computer simulations have been applied to acquire the information.[14] Nevertheless, due to the constraints of computation power and methodologies, the knowledge obtained is still limited. It is therefore of critical importance to develop a new methodology to "simulate" or "monitor" the atomic/molecular dynamic process of the nucleation and growth of crystals.[15]

The purpose of this paper is to provide an overview on the recent progress in the controlled colloidal crystallization. Our concentration will be focused on the following two aspects: the controlled colloidal crystallization as a model system to simulate and treat the kinetics of crystallization in a quantitative way, and as a template to engineer photonics crystals and to biomimic structural colors. From the fundamental point of view, some most essential issues in materials science, i.e. the dynamics of nucleation, the kink/step kinetics of crystallization, multistep crystallization, etc. will be examined. We will demonstrate that the modeling based on the electrically controlled colloidal crystallization will provide the most up-to-date knowledge on crystallization at the individual growth unit level in combination of visualization and quantitative treatment. From the aspect of applications, the fabrication of photonics crystals by colloidal crystallization will be examined. Finally, some examples of the biom,imicking of structure colors and application to textiles will be given.

Professor X. Y. Liu (Ph.D. from the Radboud University Nijmegen) has over 30 years of academic and industrial experience at various academic and industrial research institutions. He is a Professor in the National University of Singapore, and his research interests lie in the area of crystallization, soft materials, biomimetics, biophysics, etc.

Y. Y. Diao is a Ph.D. candidate. Her research interests cover the modeling and mimicking of structural colors and related optical properties of butterflies' wings by colloidal crystallization and the applications to textile industry.

2. Thermodynamic Driving Force of Colloidal Crystallization and Assembly

Notice that apart from visualization, the controlled colloidal crystallization system should demonstrate the capability of providing the controllable thermodynamics conditions for the theoretical analyses. This implies that the thermodynamic driving force should be controllable under given conditions. Regarding the colloidal crystallization, the interactions between two colloid particles play a key role. The most general equation the total free-energy difference (ΔG) between particles at infinite separation and at a separation H is obtained by adding these contributions:

$$\Delta G = \Delta G^{\mathrm{att}}(\text{van der Waals}) + \Delta G^{\mathrm{rep}}(\text{short range}) + \Delta G^{\mathrm{rep}}(\text{electrostatic}) + \Delta G^{\mathrm{rep}}(\text{steric}) + \Delta G(\text{other effects}) \quad (1)$$

where superscripts "att" and "rep" denote attraction and repulsion respectively. The consideration for the overall interactions mentioned above has been treated by the Deryagin-Landau-Verwey-Overbeek (DVLO) theory.[30] In practice, it is not necessary to consider all these contributions simultaneously, except in certain special cases. We shall here deal with the two simpler situations in which the long-range repulsive potential arises *either* from electrostatic *or* from steric contributions. Notice the way in which the double-layer repulsion depends on the ionic strength of the medium: the curves may show a high repulsive barrier at low ionic strengths, a so-called secondary minimum at intermediate ionic strengths, and a negligibly small barrier, or none at all, at higher ionic strengths. In the same way the form of the steric repulsion is determined by the nature of the interactions between the adsorbed polymer chains d the solvent. A repulsive barrier of variable range and a minimum of variable depth can result, depending on the solvent and the temperature. It follows that the interactions between colloidal particles can be turned by changing the ionic strength, pH of the solutions, or adding polymers. This implies that the "phase behavior" of such systems can be tuned by altering the above parameters.

Apart from the above mentioned forces, the interaction between colloidal particles can be induced and controlled by an alternating electric field.[15,31–45] One can tune the interaction by altering the frequency and/or the strength of the applied field. This effect can be captured by ΔG(other effects) in Equation (1). In comparison with other stimuli, the electric stimulus can be applied and switched off instantly without disturbing the original solutions. Although the interactions between colloidal particles can be of many kinds, they are basically functions of $1/r_{\mathrm{eq}}$ (r_{eq} denotes the equilibrium distance between two neighboring particles). This implies that for a given colloidal system, the interaction between two adjacent particles is fixed once r_{eq} is constant. In other words, the change of r_{eq} can reflect directly the change of inter particle interactions.

As tuning the frequency and field strength of an AC field is much easier than other conditions, we will focus on the colloidal crystallization under an AC field (i.e., **Figure 1**).[33,35,37] Nevertheless, not all ranges of frequency and intensity of the AC field can produce a crystalline assembly of particles. There exists a finite frequency range with well defined lower and upper cut-off values characteristic of particle size, charge, ionic

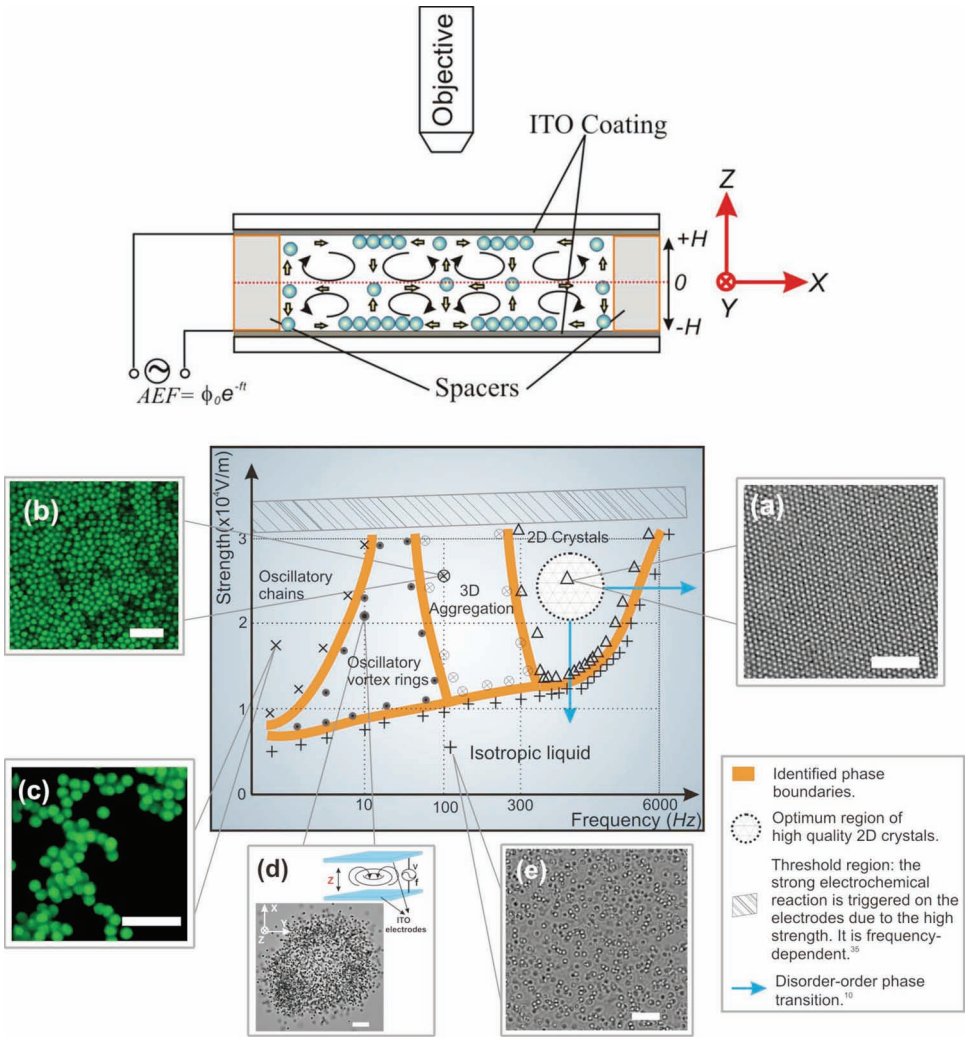

Figure 1. Top: the experimental setup. The colloidal suspension is sandwiched between two ITO-coated glass plates separated by insulating spacers. Below: The phase diagram and typical colloidal patterns induced by an AEF at room temperature. a) A 2D colloidal crystal at field strength $\sigma_E = 2.6 \times 10^4$ *V/m* and $f = 800$ Hz. b) 3D aggregation of colloidal particles, as captured by the LCSM at $\sigma_E = 2.4 \times 10^4$ *V/m* and $f = 100$ Hz. c) Static snapshot of colloidal chains by the LCSM at $\sigma_E = 1.8 \times 10^4$ *V/m* and $f = 0.1$ Hz. d) Snapshot of oscillatory vortex rings at 2.3×10^4 *V/m* and $f = 1$ Hz. e) The isotropic liquid state of colloidal suspension. Scale bars in (b) and (c) represent 5 μm, and in (a), (d) and (e) represent 10 μm. Colloidal suspension (0.1% in volume fraction) of monodisperse charged polystyrene spheres (1 μm in diameter) is confined to a horizontal layer between two conductive glass microscope slides. Glass spacers set the layer thickness in the cells at 2 $H = 120 \pm 5$ μm across the 1.5 cm × 1.5 cm observation area. The AEF was supplied by a waveform generator. The motions of the colloidal particles are recorded with a computer driven digital CCD camera. Reproduced with permission.[44] Copyright 2009, American Institute of Physics.

strength of the solution, pH etc. The attractive force which can overcome the interparticle electrostatic repulsion and enable 2D colloidal aggregation is widely suggested to be due to electrohydrodynamic (EHD) flow.[46,47] Fluid motion is set up by the interaction between this free charge and the lateral electric field, which is caused by the distortion of the applied field by the colloidal particles. A "phase diagram" of the electrically controlled colloidal assembly under a constant temperature is given in Figure 1.

In order to examine crystallization in a quantitative manner, the thermodynamic driving force should be well defined. The thermodynamic driving force for the phase transition (e.g., crystallization) can be defined by $\Delta\mu$, which refers to the difference between the chemical potentials μ_i^{ambient} and μ_{crystal} of a growth unit in the ambient mother and in the crystalline phase:

$$\Delta\mu = \mu_i^{\text{ambient}} - \mu_{\text{crystal}} \quad (2)$$

(Subscript *i* denotes the solute in the ambient phase.) When $\Delta\mu > 0$, the system is said to be supersaturated. This is the thermodynamic pre-condition for nucleation and growth of the crystalline phase. Conversely, when $\Delta\mu < 0$, the system is undersaturated. Under such a condition, crystals will dissolve. When $\Delta\mu = 0$, the ambient phase is in equilibrium with the crystalline phase. As for temperature *T* and pressure *P*, one has $(\mu_i^{\text{ambient}})_{\text{eq}} = \mu_{\text{crystal}}$.

$(\mu_i^{ambient})_{eq}$ is the chemical potential of a solute molecule in a state of phase equilibrium. Then for crystallization from solutions, the chemical potential of species i is given by[48,49]

$$\mu_i = \mu_i^0 + kT \ln a_i \approx \mu_i^0 + kT \ln C_i \quad (3)$$

where a_i, and C_i denote the activity and concentration of species i, respectively, and μ_i^0 denotes the standard state ($a_i = 1$) of the chemical potential of species i. This then gives rise to the thermodynamic driving force

$$\frac{\Delta\mu}{kT} = \ln \frac{a_i}{a_i^{eq}} \approx \ln \frac{C_i}{C_i^{eq}} \quad (4)$$

where a_i^{eq}, C_i^{eq} are, respectively, the equilibrium activity and concentration of species i. If we define the supersaturation for crystallization as

$$\sigma = (a_i - a_i^{eq})/a_i^{eq} \approx (C_i - C_i^{eq})/C_i^{eq} \quad (5)$$

Equation (4) can then be rewritten as

$$\Delta\mu/kT = \ln(1+\sigma) \cong \sigma \ (\text{in the case of } \sigma \ll 1) \quad (6)$$

For colloidal crystallization, the similar relationship can be found. If the interaction between the particles in the crystal phase remains constant at different field strength and frequencies, the supersaturation can be given by Equation (6) where $\sigma = (\phi - \phi_m)/\phi_m$ (ϕ and ϕ_m represent the actual concentration and the equilibrium concentration of the solute, respectively).

3. Simulations of Nucleation and Crystal Growth

Three dimensional (3D) crystallization, including colloidal crystallization, is a first-order phase transition process. It normally takes place via nucleation, followed by the growth of crystals. The nucleation of crystals will determine whether a crystalline phase will occur, and the correlation with its surroundings. On the other hand, the growth of crystals will to a large extent determine the size, morphology and perfection of crystals. Therefore, the understanding of the governing mechanism will allow us to exercise the effective control and the engineering of crystalline materials. In this sense, we will review how the electrically controlled colloidal crystallization can be applied to model the general process of crystallization, and other nonclassical phenomena, i.e., multi step nucleation, anti-templating effect etc.

3.1. Nucleation Barrier

The key step of nucleation is to overcome a potential barrier, so-called nucleation barrier, which a crystalline system in order to create a (crystalline) nucleus in the ambient phase, and which determines the rate of nucleation. As shown by **Figure 2**, the occurrence of nucleation barrier is subject to the interfacial energy. If under a certain condition the probability of creating a nucleus is uniform throughout the system, nucleation is defined as homogeneous nucleation. Otherwise, it is defined as heterogeneous nucleation. Notice that what has been mentioned above is normally referred to three dimensional (3D) nucleation. During crystal growth, the so-called two dimensional (2D) nucleation will take place at the growing crystal surfaces. When the growth of a crystal surface occurs under its critical roughening temperature, there will be a non-zero free energy, the so-called step free energy associated with the creation of a step of unit length at the surface. Such a crystal face has the atomically smooth surface. Due to the step free energy, the creation of a new layer on the existing layer of the crystal surface should overcome a free energy barrier, similar to 3D nucleation barrier. If the crystals are free of screw or mixed dislocations, they grow by the mechanism of 2D nucleation[3] and the growth rate R_g is largely determined by the 2D nucleation rate. Although they are not exactly the same, both 3D and 2D nucleation share many common features in almost all aspects.[49,50] Therefore, the analysis on 2D nucleation can be applicable to 3D nucleation, and vice versus.

As the most important factor, the nucleation rate J is determined by the height of the free energy barrier, the so-called nucleation barrier. The free energy change due to the formation of a cluster of can be found from thermodynamic considerations, since it is defined as

$$\Delta G = G_{fin} - G_{ini} \quad (7)$$

for a system at constant pressure and temperature (G_{ini} and G_{fin} denotes the Gibbs free energies of the system in the initial and final states before and after cluster formation, respectively). If M is the number of solute molecules in the system, one has then

$$\Delta G = -n\Delta\mu + \Phi_n \quad (8)$$

where Φ_n is the total surface energy of the n-sized cluster (except for the nucleation of bubbles when Φ_n contains also pressure–volume terms).The function ΔG reaches its maximum ΔG^* at $r = r_c$, or $n = n*$ (r and r_c are the radius and the critical

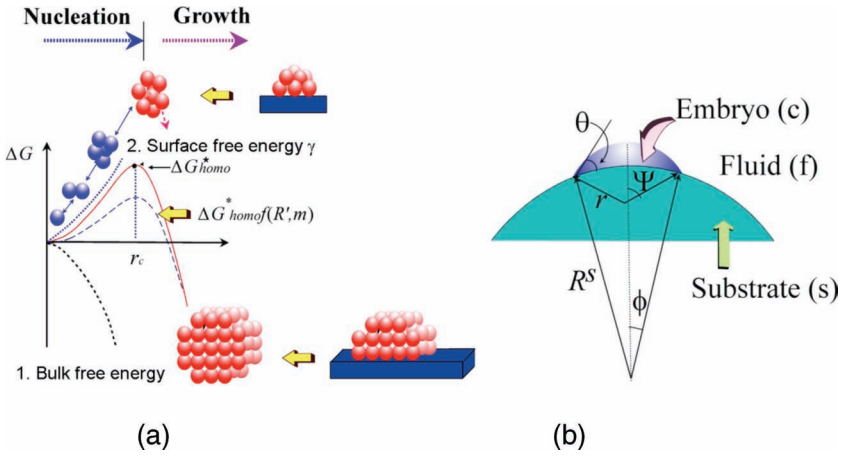

Figure 2. a) Crystallization normally takes place via nucleation, followed by the growth of crystals. Nucleation is a kinetic process of overcoming the nucleation barrier, which is the outcome of the occurrence of the surface free energy γ. b) Illustration of nucleation on a foreign particle. θ is the virtual contact angle between nucleating phase and substrate. Reproduced with permission.[27] Copyright 2004, Springer.

radius of the cluster, respectively). A cluster of n^* molecules is a critical nucleus, r_c is the radius of curvature of that critical nucleus, and ΔG^* is the nucleation barrier.

The occurrence of a foreign body in the system normally reduces the interfacial (or surface) free energy; therefore it will also lower the nucleation barrier. Let ΔG^*_{homo} be the homogeneous nucleation barrier, and $\Delta G^*_{\text{heter}}$ be the heterogeneous nucleation barrier, an interfacial correlation factor f describing the lowering of the nucleation barrier due to the action of a foreign body can be defined:

$$f = \Delta G^*_{\text{heter}} / \Delta G^*_{\text{homo}} \tag{9}$$

As shown in Figure 2b, we assume that nucleation occurs on a foreign body with a radius of R^s. The fluid phase is denoted by subscript f, the crystalline phase by c and the foreign body by s. If we denote the volume by V and the surface area of the foreign body by S, then the free energy of forming a cluster of radius r on a foreign particle of radius R^s is given, according to Equation (8), by

$$\Delta G = -\Delta\mu V_c/\Omega + \gamma_{\text{cf}} S_{\text{cf}} + (\gamma_{\text{sf}} - \gamma_{\text{sc}}) S_{\text{sc}} \tag{10}$$

where γ_{ij} is the surface free energy between phases i and j and Ω is the volume per structural unit. We have then

$$m = (\gamma_{\text{sf}} - \gamma_{\text{sc}})/\gamma_{\text{cf}} \approx \cos\theta, (-1 \le m \le 1) \tag{11}$$

To evaluate the critical free energy $\Delta G^*_{\text{heter}}$, we can substitute Equation (11) and the expressions of V_c, S_{cf} and S_{sc} into (10) and require that

$$(\partial \Delta G/\partial r) = 0 \tag{12}$$

A critical nucleus is a stable nucleus with a maximum curvature for a given thermodynamic condition. Given a certain experimental condition, the size of the critical nucleus is the same for homogeneous and heterogeneous nucleation due to the Gibbs-Thamson effect.[52–55] We have then[51,53,54] the radius of critical nuclei,

$$r_c = 2\Omega\gamma_{\text{cf}}/\Delta\mu \tag{13}$$

Referring to Figure 2c and taking

$$R' = R^s/r_c = R^s \Delta\mu/\Omega\gamma_{\text{cf}} = R^s kT \ln(1+\sigma)/\Omega\gamma_{\text{cf}} \tag{14}$$

the free energy of formation of a critical nucleus is given according to Equation (9) by

$$\Delta G^*_{\text{heter}} = \Delta G^*_{\text{homo}} f(m, R') \tag{15}$$

with

$$\Delta G^*_{\text{homo}} = \frac{16\pi\gamma_{\text{cf}}^3\Omega^2}{3[kT\ln(1+\sigma)]^2} \tag{16}$$

$$f(m, R') = \frac{1}{2} + \frac{1}{2}\left(\frac{1-mR'}{w}\right)^2 + \frac{1}{2}R'^3\left[2 - 3\left(\frac{R'-m}{w}\right) + \left(\frac{R'-m}{w}\right)^2\right] + \frac{3}{2}mR'^2\left(\frac{R'-m}{w} - 1\right) \tag{17}$$

and

$$w = [1 + (R')^2 - - 2R'm]^{1/2} \tag{18}$$

Here R' is actually the dimensionless radius of curvature of the substrate in reference to the radius of the critical nucleus r_c. Note that the factor $f(m,R')$ varies from 1 to 0. Obviously, this factor plays an important role in the determination of the heterogeneous nucleation barrier $\Delta G^*_{\text{heter}}$. One can see from Equation (9) that the influence of foreign particles on the nucleation barrier can be fully characterized by this factor.

Figure 3a shows $f(m,R')$ as a function of R' for a given m. When $R' \to 0$, $f(m, R') = 1$, implying that the foreign body "vanishes" completely as a nucleating substrate. In practice, if foreign bodies are too small, e.g., clusters of several molecules, nucleation on these substrates will not be stable. Then, they play no role in lowering the nucleation barrier. On the other hand, if $R' >> 1$, the foreign body can be treated as a flat substrate with respect to the critical nuclei. In this case, $f(m,R') = f(m)$ is solely a function of m, and Equation (17) is then reduced to

$$f(m, R') = f(m) = \frac{1}{4}(2 - 3m + m^3) \tag{19}$$

$f(m)$ as a function of m is given in Figure 3b.

3.2. Kinetics of Nucleation

The nucleation process is visualized as follows: on the substrate surface, some molecular processes occur due to transient visiting molecules which adsorb, form short lived unions, breakup, desorb etc.. An instantaneous census would show some distributions of subcritical nuclei (or clusters) with 1,2,3,…. molecules per cluster (c.f. Figure 2a).

Experimentally, the "atomic" process has never been observed in-situ before till a 2D nucleation process was monitored in the system of charged PS spheres driven by the alternating field with a fixed field strength and a frequency (ie. Figure 1).[15,58] A typical process of nucleation has been presented in **Figure 4**. On the electrode surfaces, the concentration of particles was supersaturated and the particles started to form the nuclei (Figures 4a & b, where we represented crystal-like particles as blue spheres). The nucleus in red circle kept growing whatever its state was pre- or post-nucleation; the nucleus in green circle shrank far more frequently than they grow (Figures 4c–e). In Figure 4f, the plots reflected the evolution of size of two adjacent nuclei during the process of pre-nucleation. One nucleus was growing larger and larger when its size is larger than the critical size. Moreover, the other nucleus was shrinking before reaching the critical size. This implies that nucleation is a number of simultaneous fluctuating assembly-disassembly events. A successful nucleation process corresponds to one of such events which can survive to it reaches the size of critical nuclei.[54]

For the formation of 2D nucleation of with n^* molecules, the homogeneous nucleation energy $[\Delta G^*_{\text{homo}}]_{2D}$ and the radius of critical size $(r_c)_{2D}$ are given by Equations (20,21), respectively,[15]

$$[\Delta G^*_{\text{homo}}]2D = \pi\Omega(\gamma_{\text{step}})^2/\Delta\mu \tag{20}$$

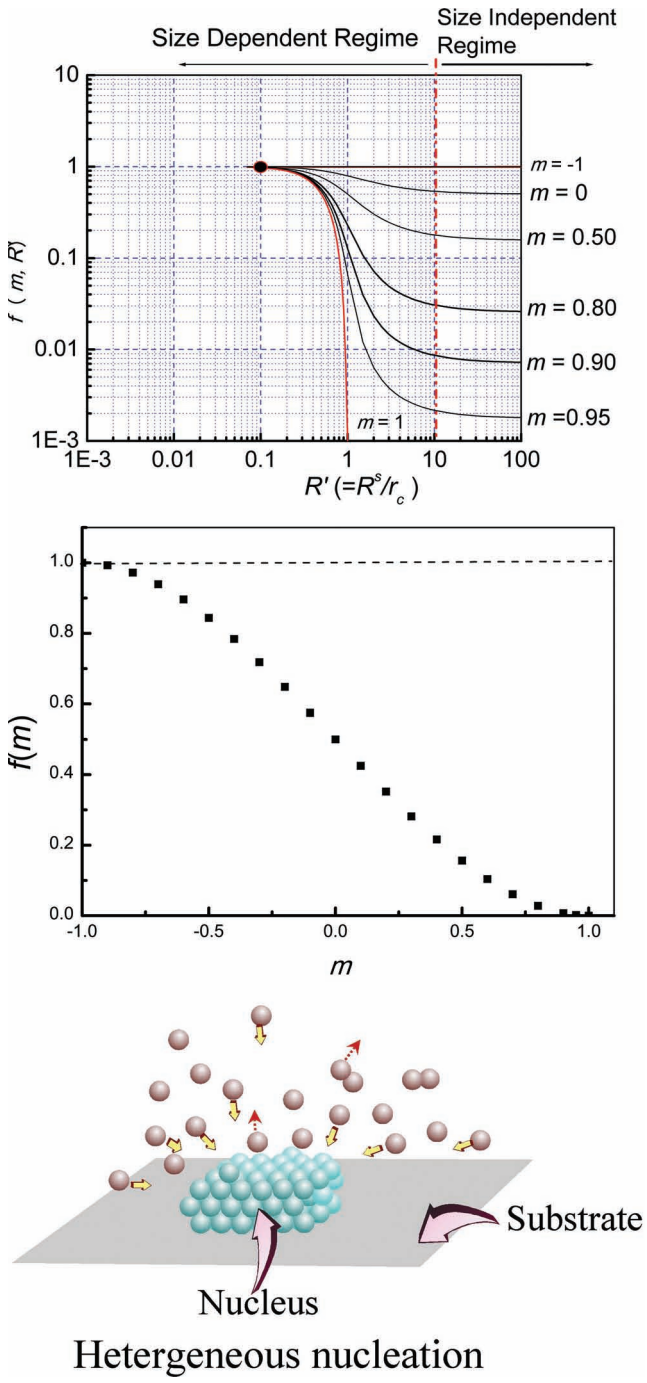

Figure 3. a) Dependence of the interfacial correlation function $f(m,R')$ on m and R'. b) Measured $f(m,R')$ in ice nucleation.[55–57] Dependence of the interfacial correlation function $f(m,R') = f(m)$ on m at $R' >> 10$. c) Schematic illustration of the shadow effect of the substrate in heterogonous nucleation. The presence of the substrate blocks the collision of growth units onto the surface of the nucleus. Reproduced with permission.[27] Copyright 2004, Springer.

$$[r_c]_{2D} = \Omega\gamma_{step}/\Delta\mu \tag{21}$$

where γ_{step} is the crystal–liquid interfacial edge free energy.

The widely accepted kinetic model of nucleation (within the cluster approach) was used first by Farkas[21] in 1927. It is based on the Szilard scheme of successive "chain reaction" between monomer molecules and n-sized clusters:

$$\text{Monomer} \rightleftharpoons \text{Dimer} \ldots \rightleftharpoons (n-1)\text{mer} \rightleftharpoons n-\text{mer} \rightleftharpoons (n+1)\text{mer} \ldots \tag{22}$$

A master equation for the concentration $Z_n(t)$ of the n-sized clusters at time t is written in the form of a continuity equation[59,60]

$$dZ_n/dt = J_{n-1} - J_n \tag{23}$$

where J_n is the flux through point n on the size axis. Thus in this formulation J is the flux through the nucleus size n^*, i.e., $J \sim J_{n*}(t)$, so that so that a time dependence is introduced in the nucleation rate.

The basic problem in the nucleation kinetics is to solve the master Equation (22) in the unknown cluster size distribution $Zn(t)$, since knowing $Zn(t)$ allows the determination of the nucleation rate. There exist three physically distinct states of the system which are of particular interest: the equilibrium, the stationary (or steady) and the nonstationary states. In the following, we will briefly discuss the equilibrium and the nonstationary states. the concentration will focus more on the steady state.

3.2.1. Equilibrium State

In equilibrium $dZ_n/dt = 0$ and $J_n = 0$. Then $Z_n = C_n$ is the equilibrium cluster size distribution. (C_n is the equilibrium concentration of n-sized clusters.) According to the Boltzmann law, one can easily obtain:

$$(C_n/Z) = (C_1/\Sigma)^n \exp(-\Delta G_n/kT) \tag{24}$$

(for all n; n = 2,3,4,…) with the effective total number of "molecules" per unit volume:

Let κ_n be the rate of molecule addition. That is,

$$k_n = \beta_{kink} K_n \tag{25}$$

where K_n is the collision rate of monomers with an n-sized cluster, and β_{kink} the conversion probability. Also let κ_n' be the rate at which the cluster lose molecules. Obviously, at the equilibrium state, one has the detailed balance between the growth and disintegration of clusters,

$$k_n C_n - k'_{n+1} C_{n+1} = 0 \tag{26}$$

Since $\Delta G^*_{heter}(\Delta\mu)$ has a maximum at $n = n^*$, C_n displays a minimum at the critical nucleus size. The increasing, nonphysical branch of C_n at $n > n*$ reflects the fact that the mother phase is saturated.

3.2.2. Stationary (or Steady) State

In the stationary state, $dZ_n/dt = 0$. Because J_n = constant = J_{n*} = J, $Z_n \sim Z'_n$ is the steady-state cluster size distribution. The stationary nucleation rate for homogeneous nucleation is given by the Becker-Doering formula[51]

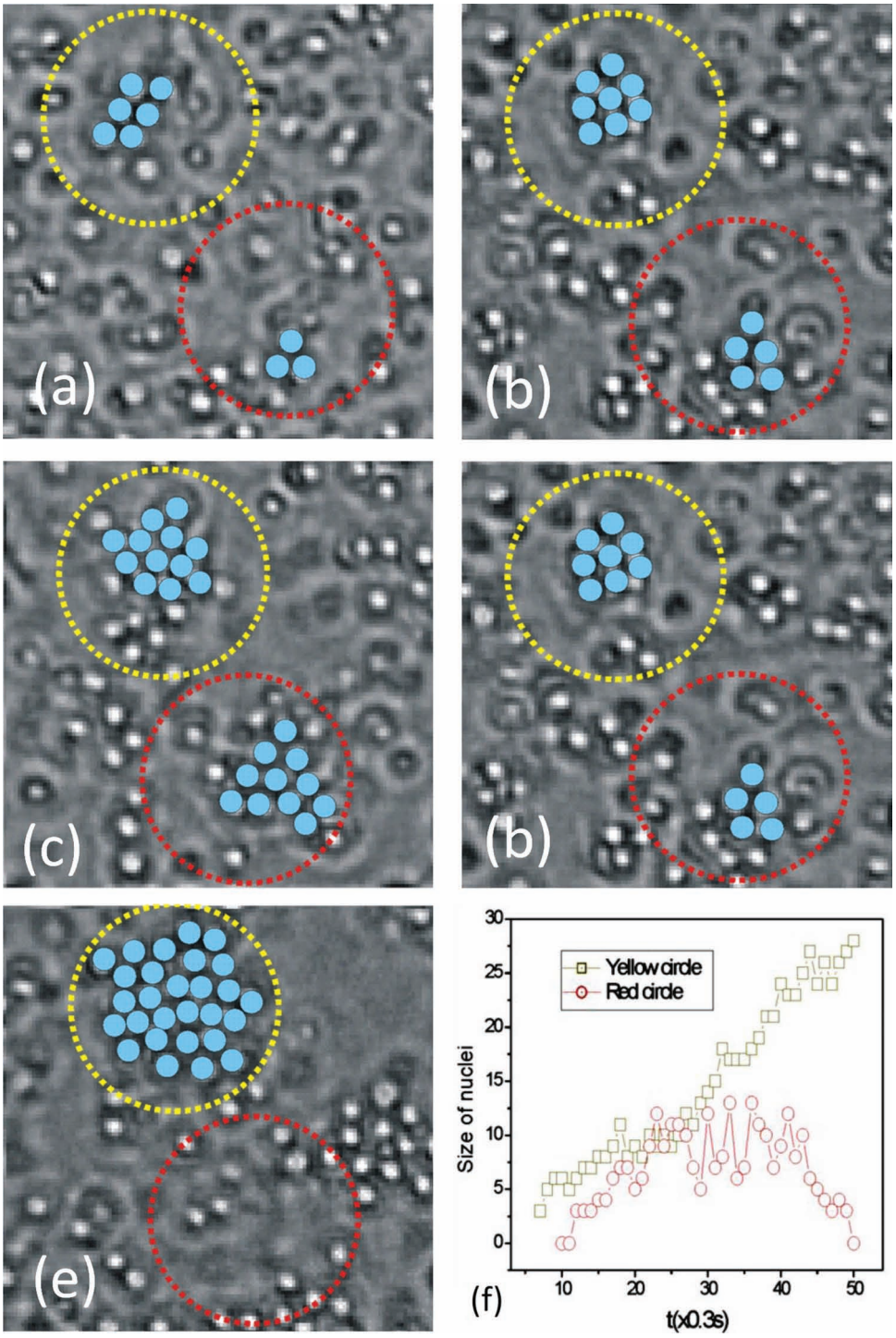

Figure 4. The snapshots of process of pre-nucleation. a) Time $t = 10\ t_0$ (t_0 is the timing interval of images, 0.3s). b) 20 t_0. c) 30 t_0. d) 40 t_0. e) 50 t_0. f) The evolution of size of two nuclei. The yellow curve represents the increasing size of nucleus in the yellow circle; the red curve represents the shrinkage of nucleus in the red circle. ($\sigma_E = 2.6 \times 10^4$ V/m, $f = 600$ Hz.[15]) Reproduced with permission.[15] Copyright 2004, Nature Publishing Group.

$$J = \frac{zK^*}{\nu_m} \exp\left(-\frac{\Delta G^*_{\text{homo}}}{kT}\right) \tag{27}$$

with

$$z = Z'_{n^*}/C_{n^*} - Z'_{n^*+1}/C_{n^*+1} \tag{28}$$

where z is the so-called Zeldovich factor,[48,59] $K^* = K_{n^*}$ is the frequency of monomer attachment to the critical nucleus, ν_m denotes the average volume of structural units in the ambient phase, and C_n is the equilibrium concentration of n-sized clusters given by,[48]

$$C_n \cong C_1 \exp(-\Delta G_n / kT) \tag{29}$$

Based on the definition of J_n, one has

$$J_n = k_n Z'_n \tag{30}$$

At the steady state, J', that is the formation rate of critical nuclei per unit volume-time around a foreign particle, is equal to the steady state growth of clusters on the surface of the particle. The nucleation rate can then be expressed in terms of

$$\begin{aligned} J' &= J_{n^*} = J_n = \text{constant} \\ &= \text{critical sized nuclei formed / unit volume} - \text{time} \equiv \ldots \\ &= k_n Z'_n - k_{n+1} Z'_{n+1} = \text{constant.} \end{aligned} \tag{31}$$

Taking into account the effect of the substrate on both the nucleation barrier and the transport process, and the fact that the average nucleation rate in the fluid phase depends on the density and size of the foreign particles present in the system, the nucleation rate is given by[48,59]

$$J = 4\pi a (R^s)^2 N^o f''(m, R') [f(m, R')]^{1/2} \times B \exp\left[-\frac{16\pi \gamma_{cf}^3 \Omega^2}{3kT[kT \ln(1+\sigma)]^2} f(m, R')\right] \tag{32}$$

with

$$B = (C_1)^2 4 D \beta_{kink} \Omega \left(\frac{\gamma_{cf}}{kT}\right)^{1/2} \tag{33}$$

$$f(m, R') = \frac{1 + (1 - R'm)/w}{2} \tag{34}$$

and

$$f(m, R') = f(m) = \frac{1}{2}(1 - m) \text{ at } R' >> 1 \tag{35}$$

where B is the kinetic constant and N° denotes the number density of the substrates (or "seeds"). The growth of nuclei is subject to the effective collision and incorporation of growth units into the surfaces of the nuclei (cf. Figure 3c). In the case of homogeneous nucleation, the growth units can be incorporated into the nuclei from all directions. However, in the case of heterogeneous nucleation, the presence of the substrate will block the collision path of the growth units to the surfaces of these nuclei from the side of the substrate (cf. Figure 3c). This is comparable to the "shadow" of the substrate cast on the surface of the nuclei. $f''(m,R')$ in the pre-exponential factor, which is the ratio between the average effective collision in the presence of substrates and that of homogeneous nucleation (i.e., in the absence of a substrate), describes this effect.

Both $f(m,R')$ and $f''(m,R')$ are functions of m and R'. When $R' \to 0$ or $m \to -1$, $f(m,R')$, $f''(m,R') = 1$. This is equivalent to the case of homogeneous nucleation. In the case where $m \to 1$ and $R >> 1$, one has $f(m,R')$, $f''(m,R') = 0$. Normally, heterogeneous nucleation occurs in the range between 1 and –1, or $f(m,R')$ between 0 and 1, depending on the nature of the substrate surface and the supersaturation.

Note that for homogeneous nucleation, one has $f''(m,R') = f(m,R') = 1$, and $4\pi a(R^s)^2 N^o \to 1$. In this case, Equation (32) is converted to

$$J = B \exp\left[-\frac{16\pi \gamma_{cf}^3 \Omega^2}{3kT[kT \ln(1+\sigma)]^2}\right] \tag{36}$$

This implies that Equation (29) is applicable to both homogenous and heterogeneous nucleation.

Similar to 3D nucleation, 2D nucleation can also adopt a similar form,[48]

$$J_{2D} = \left\{\frac{2D_s C_1^2}{\pi}\left[\frac{\Omega \ln(1+\sigma)}{h}\right]^{1/2} \exp\left(-\frac{\Omega(\gamma_{cf}^{step})^2 \pi h}{(kT)^2 \ln(1+\sigma)} f_{2D}(m_{2D}, R_{2D})\right)\right\} \times \beta_{kink} \delta(m_{2D}, R'_{2D}, R^s, N^o) \tag{37}$$

with

$$\delta(m_{2D}, R'_{2D}, R^s, N^o) = \left\{\frac{\psi}{\pi} N^o \pi a R'_{2D}\left[f_{2D}\left(m_{2D}, R'_{2D},\right)\right]^{1/2}\right\} \tag{38}$$

where D_s denotes the surface diffusivity. In the case of 2D homogeneous nucleation, one has $\delta(m_{2D}, R'_{2D}, R^s, N^o) = f_{2D}(m_{2D}, R'_{2D})$, Equation (37) can be simplified as:

$$J_{2D} = \left\{\frac{2D_s n_1^2}{\pi}\left[\frac{\Omega \ln(1+\sigma)}{h}\right]^{1/2} \exp\left(-\frac{\pi \Omega h \gamma^2}{(kT)^2 \ln(1+\sigma)}\right)\right\} \beta'_{kink} \tag{39}$$

Here n_1 is the number of single particles (monomers), β_{kink} is the sticking possibility.

3.2.3. Non-Stationary (or Non- Steady) State

When the nucleation is nonstationary, $dZ_n/dt \neq 0$ and flux J_n is a function of both n and t. The nucleation rate is then time-dependent and this nonstationary nucleation rate $J_{nonst}(t) = J_{n^*}(t)$. In other word, $J_{nonst}(t)$ will change with time.

3.2.4. Experimental Verification of Nucleation Kinetics Based on Colloidal Crystallization

Although theoretical analysis on the above states of nucleation has been published for long time, experimental verification in particular the direct measurement for the distribution of subcritical nuclei had never been achieved till recently when the controlled 2D colloidal nucleation was carried out.[15] By measuring the size distribution of subcritical nuclei on the surface of flat electrode, we observed the evolution among the different kinetics: non-stationary, stationary and equilibrium state[48] in the process of pre-nucleation. **Figure 5**a presented a typical distribution at different time. Once applied the driving force, the small nuclei formed. Subsequently the cluster size exceeded the critical size of nuclei, the nuclei were growing to the crystallites gradually. Figure 5a reflected this image of nucleation kinetics. Here we defined a transient point $n^*(t)$ that where the size distribution approached to a steady number of clusters in the nucleation (see Figure 5a inset).

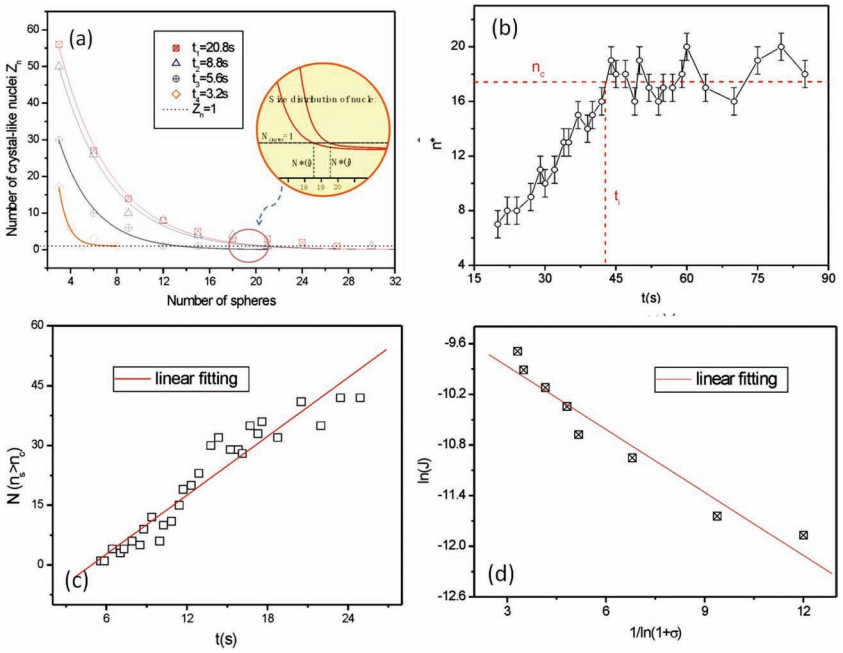

Figure 5. Statistical measurement of parameters of nucleation kinetics. a) The typical size distribution of subcritical nuclei versus time ($\sigma_E = 2.6 \times 10^4$ *V/m f* = 600 Hz.). b) n^* (*t*) versus time. After the induction time, n^* (*t*) becomes stable. The critical size can be determined. c) The number of nuclei which size is larger than the critical size in different time. We can measure the nucleation rate in the unit area according to the slope of linear fitting of this curve. d) The nucleation rate under the different supersaturation (driving force). The straightfitting line is based on Equation (39). From Equation (39), we also can get the line tension of interface. The value of γ_{step} is 0.50 *kT/ a* (*a* is the diameter of colloidal particles) which is agreement with the measurements. Reproduced with permission.[15] Copyright 2004, Nature Publishing Group.

We can obtain the following results from Figure 5:

1. At the beginning of nucleation, the system starts from a non-stationary states stationary (*t* = 3.2 s) and gradually approaches toward the stationary state (*t* > 20 s) in which the distribution of nucleating clusters Z_n is independent of time.
2. A nucleation event is successful once the distribution of nucleating clusters $Z_{n^*} = 1$ in any time. Therefore, the cluster size at $Z_n = 1$ can be defined as the critical size of nucleation n^*.
3. Before reaching the stationary state, n^* is time-dependent. Only after the stationary state, the critical size of nucleus n^* can acquire a constant value (Figure 5b). In other words, it only makes sense to discussion the critical size of nucleus at the stationary state.

Two dimensional colloidal crystallization enables us to determine the critical size of individual nuclei, and verify the nucleation model (Equation (39)) directly. In Figure 5c, we plotted and the curves and determined the average nucleation rate in the unit area of surface according to the fitting slope of curves. Figure 5d presents the nucleation rate density under the different driving force. The linear fitting of the plot of $\ln(J) \sim 1/\ln(1 + \sigma)$ indicates that Equation (39) can be applied to quantify the nucleation kinetics of 2D nucleation.

3.3. Initial Stage of Nucleation: Is Classical Nucleation Theory Accurate?

Although the basic treatments of classic nucleation theories have been approved to be correct as shown in Sec. 3.2.3, some aspects of nucleation remain unclear. In the analysis of nucleation kinetics in 3.2, the structure of crystal nuclei is supposed to be identical to the bulk crystals. Is this assumption correct? If not, what are the consequences? In the following, we will discuss the interfacial structural evolution during nucleation, and the impact of the interfacial structure of nucleating clusters on the nucleation energy barrier, in terms of 2D colloidal crystallization model system.

To quantify the ordering of two dimensional crystal nuclei, a local two-dimensional bond-order parameter is defined as follows:[36–39]

$$\psi_6(r_i) = M^{-1} \left| \sum_j e^{i6\theta_{ij}} \right| \quad (40)$$

where r_i is the center of particle *i*, and θ_{ij} is the angle subtended between the vector from particle *i* to its j^{th} nearest neighbor and the arbitrarily chosen *x* axis. *M* is the number of nearest neighbors of particle *i*. The mean value of $\psi_6(r_i)$ for crystalline structures obtained from the experiments is 0.8 which is taken as the criterion for a crystal-like particle.

Figure 6a reveals that at relatively low supersaturations, the structure of crystalline clusters is a bit fluid-like and more disordered at the beginning, and gradually approaches to the ordered structure in the bulk crystalline phase as the size close to the critical size of nuclei. The transition from the initial metastable structure to the final stable structure is a continuous process.

On the other hand, at high supersaturations (decreasing frequency gives rise to the increase of supersaturation),[61] the Figure 6b shows the structural transition occurring under conditions of *f* = 3000 Hz and V_{pp} = 2.5 V. Different from the behavior of $\langle\psi_6\rangle$ in Figure 6a, $\langle\psi_6\rangle$ can be as high as 0.8 instantaneously even before it reaches its transition size (~30) (in Figure 6b(i)). This implies that the nucleus can have a crystalline structure even before it becomes stable in structure. Nevertheless, the crystalline structure of the precritical nuclei is transient and fluctuated. In Figure 6b(ii) & (iv), the structure of the nucleus is ordered. In the subsequent seconds, as shown in Figure 6b(iii) & (v), it becomes disordered again. Only as the size is beyond the critical size ~30, the crystalline structure becomes stable. As the supersaturation is increased further by decreasing frequency, $\langle\psi_6\rangle$ remains more or less 0.8 in the whole growth process from the beginning, and crystal nuclei are initially created with a crystalline structure as suggested by classical nucleation theory.[43]

The results in Figure 6 indicate that the initial structure of crystal nuclei and the structural evolution of crystal nuclei are supersatruation-dependent. At low supersaturations, a metastable liquid-like structure is likely to occur first. This is because at the nucleation barrier is very high at low supersaturations (cf. Equations (16) and (21)). The occurrence of the metastable structure at the nuclei may help to reduce the nucleation

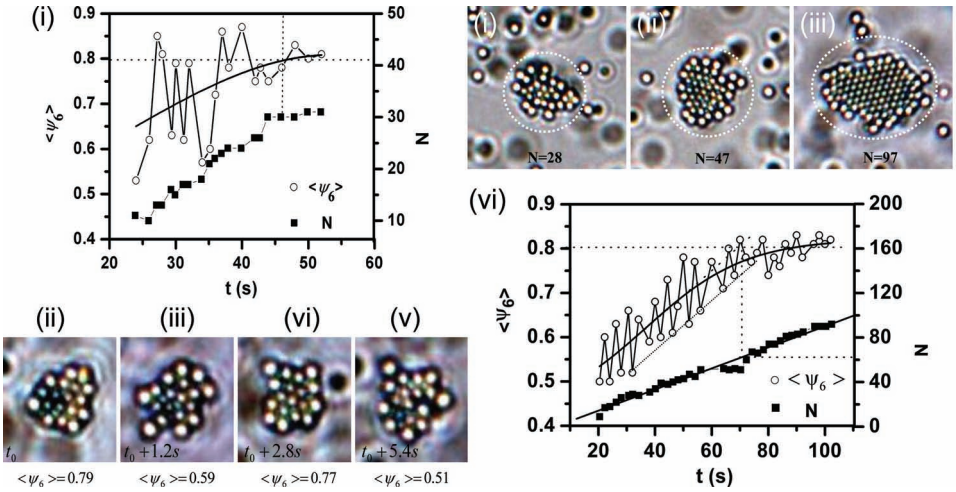

Figure 6. a) Structural evolution of nuclei under conditions of V_{pp} = 2.5V, f = 5000 Hz. (i) Initial structure of nuclei is liquid-like. (ii) As the nucleus grows, its core first becomes ordered with the exterior layer remaining liquid-like. (iii) The nuclei become completely ordered after they exceed a critical size. (iv) $<\psi_6>$ is a function of nuclei size N. Monodisperse colloidal particles (polystyrene spheres of diameter 0.99 mm, polydispersity <5%, Bangs Laboratories) were dispersed uniformly in deionized water. The colloidal suspension was then sealed between two parallel horizontal conducting glass plates coated with indium tin oxide (ITO).The gap between the two glass plates is $H = 120 \pm 5$ mm. The dynamic process is recorded by a digital camera (CCD) for analysis. AEF = alternating electric field. b) Phase diagram of the system when the concentration of Na_2SO_4 is 2×10^{-4} M. V_{pp} = peak to peak voltage. Due to the nature of 2D crystals, $<\psi_6>$ for a perfect 2D crystal is 0.8. (b) Transient crystalline structure of nuclei under condition of V_{pp} = 2.5V, f = 3000 Hz. (i): Fluctuation of order parameter during the growth. (ii), (iii): Due to the structural fluctuation, nuclei can have a transient crystalline structure. (iv), (v) Liquid-like structure displayed by precritical nuclei. Reproduced with permission.[44]

barrier,[62,63] therefore, it is kinetically more favorable. In On the other hand, the nucleation barrier becomes much lower at higher supersaturations (cf. Equations (16) and (21)), the structural relaxation of nuclei is not kinetically very favorable. Therefore, the structure of pre-nucleation clusters can be as ordered as that of the bulk crystalline phase.

The analyses on the kinetic data[32,34,43] confirm that at low supersaturations, the evolution of nuclei from a liquid-like structure to a crystal-like structure will effectively reduce nucleation barrier, and facilitate the nucleation dynamics. In other words, at low supersaturations, the classical nucleation theories (CNT) overestimate the nucleation barrier. At high supersaturations, as the nucleation barrier decreases substantially. Adopting the structure of the bulk crystals during nucleation needs not to be energetically unfavorable. Therefore, the dynamic behavior predicted by the classical nucleation theories (CNT) becomes valid.

3.4. Multi-Step Nucleation/Crystallization

The results presented in Section 3.3. demonstrate that at low supersaturations, the classical nucleation theories (CNT) may overestimate the nucleation barrier. It follows that relaxing the interfacial structure of crystalline nuclei can reduce the nucleation barrier and facilitate the nucleation kinetics. In nature, there are some other ways to facilitate the nucleation kinetics. It is found that in protein crystallization,[28,64–66] biomineralization, etc., crystallization often occurs via metastable phases. A typical stepwise crystallization is the so-called two-step crystallization (TSC).[67] According to TSC, dense amorphous droplets are first formed from the mother phase; crystalline nuclei are then created from the droplets. For instance, during the formation of calcite in sea urchin larvae, a transient amorphous phase is formed first, before the final crystal phase is reached.[68,69] Similarly, a transient amorphous phase is also identified during the formation of aragonite controlled by mollusk bivalve larvae.[70] Recently, the similar process has also been observed for the hydroxylapatite (HAP) formation from a simulated body fluid.[71] It is widely believed that in biological systems, the development of crystalline structures characterized by well-defined shape and size is essentially facilitated by the occurrence of transient amorphous phases.[69–71] In fact, recent studies indicated that TSC may be a mechanism underlying most crystallization occurring in typical atomic systems.[62,72,73]

TSC has attracted much attention in the past decade due to its importance in both scientific and technological point of view. However, the understanding of TSC remain to be insufficient. A key challenge is that the kinetics creating the initial crystalline nuclei from the dense droplets is unclear and thus it is no way to predict the overall nucleation rate J_c of crystals. In this section, we will recap the multi-step crystallization (MSC) in the colloidal model system. The kinetics of MSC is discussed and a mathematical method is developed to address the local nucleation rate J_c of crystal in the droplets.

A typical process of MSC, observed under conditions of V_{pp} = 2.0 V and f = 800 Hz, is presented in **Figure 7**. Colloidal particles in the initial mother solution are uniformly distributed in the solution (i.e., Figure 7a).

When an AEF is applied to the system, colloidal particles are transported onto the glass surface where they first form dense droplets (Figure 7b). Subsequently, a few sub crystal nuclei are created from the droplets as illustrated by Figure 7c. These subnuclei are not stable and will dissolve soon after they are created. Experimentally, it is found that the crystalline

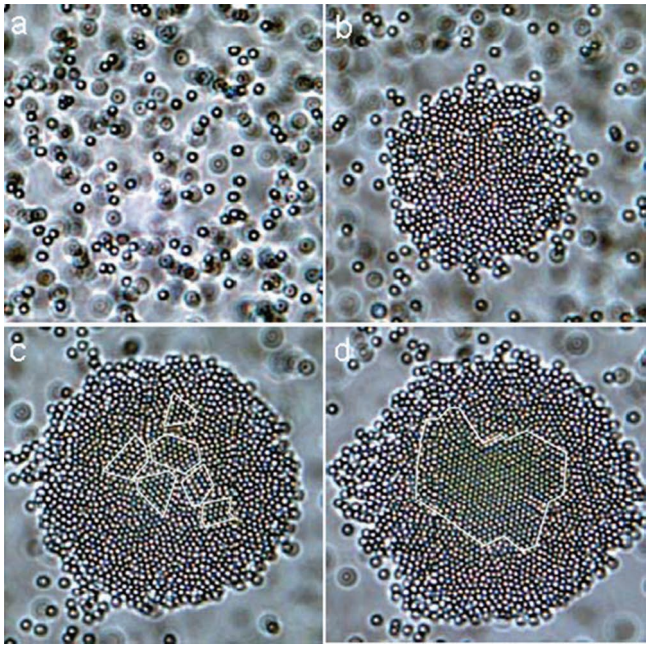

Figure 7. Multi-step crystallization observed at 800 Hz and 2.0 V: a) Initial dilute liquid phase. b) Amorphous dense droplets are first created from the mother phase. c) A few sub crystal nuclei are created from the amorphous phase. d) A stable crystal is formed from the dense droplets. Colloidal suspension is sealed between two pieces of ITO-coated conducting glass plates separated by insulating spacers. The gap between the two glass plates is $H = 120 \pm 5$ μm. The dynamic process is recorded by a digital camera for analysis. b) Phase diagram of the colloidal suspension. Monodisperse colloidal particles (polystyrene spheres of diameter 0.99 μm, polydispersity < 5%, Bangs Laboratories) are dispersed uniformly in deionized water. In the case, the volume fraction 0.03% of colloidal solid is chosen and the surface potential of the colloidal spheres is adjusted to –72 mv by Na_2SO_4 (10^{-4} M). The pH of the suspension is measured at 6.35. Monodisperse colloidal particles are dispersed uniformly in deionized water. Reproduced with permission.[38] Copyright 2003, American Chemical Society.

nuclei in the droplets have to acquire a critical size N^*_{cry} before they can grow stably in the droplets as shown in Figure 7d. In the experiments, every droplet can produce only one stable crystal. Moreover, to form a stable crystal beyond N^*_{cry}, the droplets have to first acquire a critical size N^*. It is found that although at an early stage, many small dense droplets are created, only three or four out of twenty droplets can reach the critical size N^* and develop successfully into a stable crystal. This is consistent with previous observations in protein crystallization.[74,75] However, it is contradicting with the assumption by Kashchiev et al.[76] A detailed analysis on the overall nucleation rate J_c of MSC., determined by the local rate J_c in the individual dense droplets is given in the literature.[52]

In general, the multistep crystallization (MSC) in a colloidal model system indicates that amorphous dense droplets are first nucleated from the mother phase. Subsequently, a few unstable subcrystalline nuclei can be created simultaneously by fluctuation from the tiny dense droplets, which is different from previous theoretical predictions. Notice that it is necessary for these crystalline nuclei to reach a critical size N_{cry} to become stable. However, in contrast to subcrystalline nuclei, a stable mature crystalline nucleus is not created by fluctuation but by coalescence of subcrystalline nuclei, which is unexpected. To accommodate a mature crystalline nucleus larger than the critical size N_{cry}, the dense droplets have to first acquire a critical size $N*$. This implies that only a fraction of amorphous dense droplets can serve as a precursor of crystal nucleation. As an outcome, the overall nucleation rate of the crystalline phase is, to a large extent, determined by the nucleation rate of crystals in the dense droplets, which is much lower than the previous theoretical expectation. The calculations indicate that the multi step crystallization is indeed kinetically more favorable than one step crystallization under the given conditions.[39]

3.5. Surface Kinetics of Crystallization

Crystallization takes place at the interfacial region between the crystalline region and the fluid phase, the interfacial kinetics plays an essential role in controlling nucleation, crystal growth, and related phenomena, ie. surface roughening, growth morphology, polymorphism, etc.[15,75–78] The electrically controlled colloidal crystallization will obviously provide a unique approach to model and "reveal" the processes at the interfacial layer.

3.5.1. Step Kinetics of Crystal Surface

Crystal surfaces, where the steps and kinks occur, can be treated as 2D crystals. 2D colloidal crystals can then be adopted to model the top layers of crystal surfaces. In **Figure 8**a, the colloidal lines can be introduced as the pre existing steps to examine step kinetics. A colloidal line composed of 1.8 μm PS particles was pre-deposited on the bottom ITO electrode using a controlled dewetting lithography method as a template to match the size of the crystallizing colloidal particles.[40–42]

In the classical treatment of nucleation and growth, researchers normally simplify the growth units as monomers. Then the questions arise: will the growth units be clusters (or *n*-mers), and if yes, how the incorporating clusters fit to the structure of the crystals? Would they remain as defects, i.e., inclusions? To address these questions, the evolution of 2D colloidal crystal growth at the colloidal lines as templates (Figure 8) was monitored. At the very initial stage, the colloidal particles were randomly dispersed in the cell (0s), upon the application of the AEF of frequency $f = 800$ Hz and field strength $\sigma_E = 4.0 \times 10^4$ V/m, the free-dispersed colloidal particles in the bulk fluid phase were transported to the electrode surface and accumulated near the colloidal lines directed by the electric-field-induced attractions.[40–42] A rapid increase of superpersaturation generates a large number of colloidal particles clusters in the front of the step (Figure 8b, $t = 2.6$ s). Subsequently, the clusters can grow further in the bulk fluid phase, as shown in Figure 8b ($t = 15.6$ s), then were transported toward the growing front at the template. During the incorporation process, the downward funneling (DF) effect[42,43] was observed: particles deposited beyond an island edge would funnel down to the lowest positions in the vicinity of the deposition site. The evolution of two typical incorporated clusters is highlighted by the red and yellow particles in Figure 8b, respectively. Although these clusters were randomly oriented in the bulk fluid phase ($t = 15.6$ s,

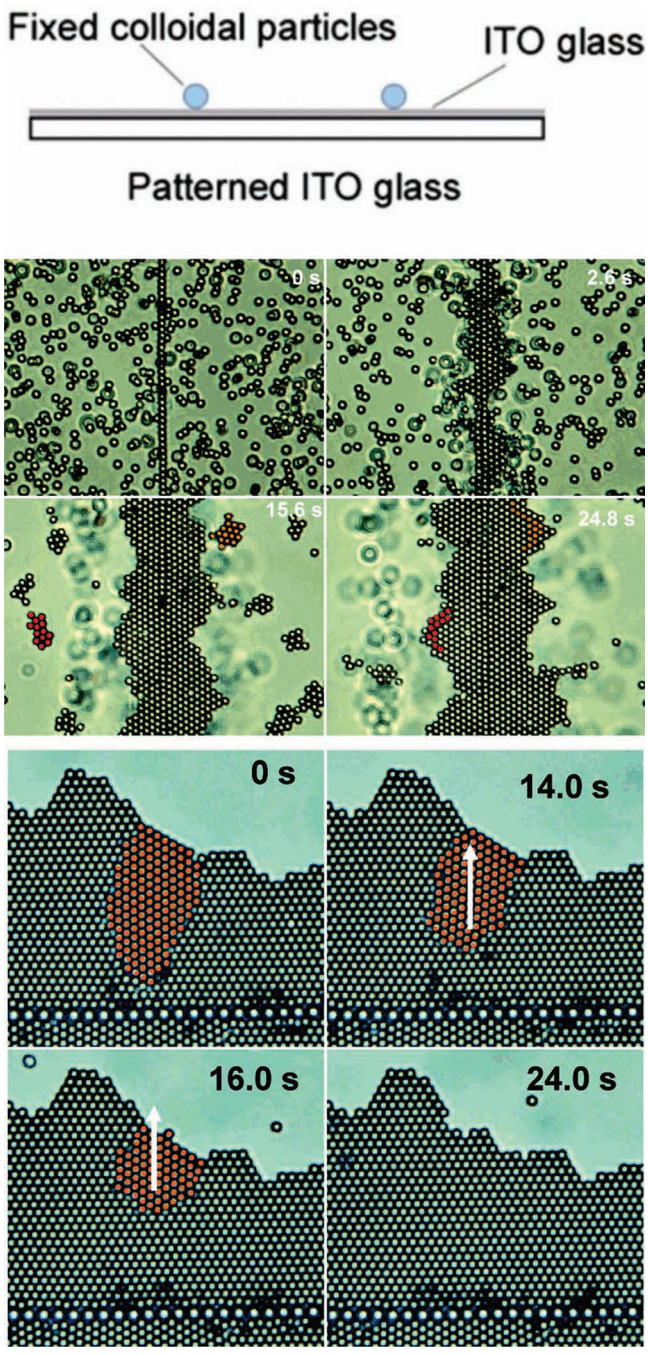

Figure 8. a) Schematic illustration of the epitaxial assembly of 2D colloidal crystals under an AEF.[39–42] b) High-resolution time snapshots of the epitaxial crystallization of 1.8 μm colloidal particles using a 1.8 μm colloidal particle line as a template, under the AEF of frequency $f = 800$ Hz and field strength $\sigma_E = 4.0 \times 10^4$ V/ m. The bright dots correspond to the well-focused spheres that are assembled on the bottom electrode. The dark dots correspond to the ill-focused spheres, which are suspended in the bulk solution. c) The evolution of a mis-orientated grain in a colloidal crystal composed of 1.8 μm colloidal particles and a 3.0 μm artificial linear defect, during a controllable annealing process by tuning the frequency from 1000 to 600 Hz. The aqueous suspension of the 1.8 μm polystyrene (PS) particles was sandwiched and sealed in a glass cell composed of two pieces of conductive indium tin oxide (ITO) electrodes. Reproduced with permission.[42] Copyright 2009, American Chemical Society.

and $t = 24.8$ s), they would rearrange themselves to find their optimal positions and orientations when they deposited on the islands, forming a single colloidal crystal with a well-defined orientation with respect to the colloid line. Obviously, this self orientation process of incoporating clusters maintains the growing crystals in a high degree of ordering and perfection. Of course, if the incoming flux of grow units is too rapid, i.e., at high supersaturations, and the clusters are buried into the crystals before the re- orientation takes place, the defects can then be introduced.

Further experimental observations show that the degree of perfection of the colloidal crystals changes with the frequency of the AEF. The high-quality oriented single colloidal crystals were obtained in the low-frequency range (400–800 Hz, the low driving force regime). When the frequency increased to the high range (1000–2000 Hz, the high driving force regime), the orientation order parameter gradually decreased, and the vacancy concentration increased. This may also result in the supersaturation-driven interfacial structure mismatch nucleation,[79] which will be highlighted in the following section.

It is commonly known that the post treatment of crystallization will help anneal defects, and improve the perfection of crystals. To examine this process, a well-defined linear defect was introduced inside a 2D colloidal crystal. Figure 8c shows a 1.8 μm colloidal crystal embedded with a 3.0 μm linear defect (formed under the AEF of frequency f = 1000 Hz and field strength $\sigma_E = 4.0 \times 10^4$ V/m) and its time evolution by tuning the frequency from 1000 to 600 Hz. As can be observed, there existed a mis-orientated domain near the colloidal line template due to lattice-mismatch-induced disordering. Since the particle interactions can be precisely modulated by tuning the frequency of the AEF, these unwanted defects can be further eliminated through electrically induced annealing in the frequency range where the interlayer transport of colloidal particles is active. As can be seen in Figure 8c, when the frequency was tuned from 1000 to 600 Hz, the exiting grain boundary moved away from the template, gradually shrunk with time, and then disappeared without generating new ones. Finally, a highly ordered, single colloidal crystal with a well-defined domain will be obtained. This effect can be regarded as self perfection.

We notice that this epitaxial templating approach enables unprecedented control over the defects inside the 2D colloidal crystals and large-area electrically reversible patterning of 2D colloidal crystals, thus expanding the potential for a wide range of practical applications, such as electrically tunable photonic waveguides and e-papers.

3.5.2. Templating and Supersaturation-Driven Interfacial Structure Mismatch Nucleation

We have demonstrated a reliable and rapid epitaxial templating approach for the controllable crystallization of large area 2D colloidal crystals with well-defined orientations, artificial defects, and patterns. We have also showed that pre-defined 1D colloidal lines or lithographically templated electrodes can be utilized to site specifically initiate the 2D colloidal nucleation and control the crystal orientation, wherein controlling an external alternating electric field (AEF) (thermodynamic driving force) allows us to precisely and conveniently manipulate the kinetic process of the crystal growth.

Notice that the occurrence of substrates will, on one hand, lower the nucleation barrier thus leading to an increase in the nucleation rate, but on the other hand it will exert a negative impact on the surface integration. Nucleation on a substrate will reduce the effective collisions of structural units to the surface of clusters (the so-called shadow effect, cf. Figure 3c). This will slow the nucleation kinetics, in contrast to the nucleation barrier lowering effect.

These two contradictory effects play different roles in different regimes. At low supersaturations, the nucleation barrier is very high (cf. Equations (15) and (16)). The nucleation rate will be substantially enhanced if the nucleation barrier is suppressed effectively ($f(m)\rightarrow 0$). Therefore, heterogeneous nucleation with a strong interaction and optimal structural match between the substrate and the nucleating phase will be kinetically favored. In this case, the nucleation of crystalline materials will be best templated by substrates capable of providing the excellent structural correlation with the crystalline phase. The structural synergy between the nucleating phase and the substrate will be optimal under this condition.

At higher supersaturations, the exponential term associated with the nucleation barrier becomes less important. Instead, *the shadow effect* of the substrate, described by the pre-exponential factors $f(m)$ and $f'(m)$ in the pre exponential term of, Equation (32) dominates the kinetics more strongly (cf. Figure 3c). Nucleation on the substrates having larger $f(m)$ and $f''(m)$ (or $m \rightarrow 0, -1$) will have a higher degree of orientational freedom (or a larger entropy). This will reduce the shadow effect of the substrate, and therefore it will become kinetically more favorable. This implies that the epitaxial template relationship between substrate and the nucleating phase cannot be maintained even for the substrates having an excellent structural match with crystalline materials, if the supersaturation is too high.

If σ progressively increases from low supersaturations to high supersaturations, nucleation will be governed by a sequence of progressive heterogeneous processes associated with increasing $f(m)$. In analogy with the above analysis, we should obtain a set of pairwise intercecting straight lines if $\ln t_s$ is plotted against $1/[\ln(1+\sigma)]^2$ (t_s: induction time; cf. **Figures 9**a and b). Since for the crystalline phase, m and $f(m)$ take on only those values which correspond to some crystallographically preferential orientations, $f(m)$ or the slope of the straight lines will take on discrete values, and $f(m)$ will increase as σ increases. A typical example is given in Figure 9, where the measured induction time is shown as a function of supersaturation for $CaCO_3$ nucleating from aqueous solutions.[53]

As shown in Figure 9a and b, the interfacial correlation factor $f(m,R')$ subsequently increases from $3.9/\rho$ to $12.5/\rho$, as supersaturation increases from 1.5 to 5. This result unambiguously confirms that the increase of supersaturation will drive the substrates/biominerals from an interfacial structural match state (a lower $f(m)$) to an interfacial structure mismatch state (a higher $f(m)$). This is referred to the *supersaturation-driven interfacial structural mismatch*.[79,80] As mentioned above, the abrupt changes from one state to the other at certain supersaturations (such as A, B, … in Figure 9) are due to the anisotropy of the crystalline phase. The templating and the supersaturation driven interfacial structure mismatch nucleation (or anti-templating) are the two contradictory effects.

Recently, the effect of supersaturation-driven interfacial structural mismatch nucleation has been found to play a very important part in the pattern formation, crystallite network formation, supramolecules soft materials formation.[27,48–50] Although the discussion based on the theoretical analysis and nucleation experiments has been given, a direct experimental verification on the templating and the supersaturation driven interfacial structural mismatch has not been acquired yet. In this regard, the epitaxial assembly method based on the crystallization of 2D colloidal crystals under an alternating electric field (AEF) is applicable to investigate this matter (Figure 9d).

To examine the ordering of the colloidal crystals at the template, the orientational order parameter $S = \frac{1}{2} \langle 3\cos^2\theta - 1\rangle$[80] is applied to characterize the uniaxial ordering of the colloidal assembly. θ is the misfit angle of the crystal domain with respect to the epitaxial colloidal line, as shown in the right inset in Figure 9e. The brackets denote an average over all of the particles in the assembly. When colloidal particles are perfectly oriented parallel to the epitaxial template, we have $S = 1$. Figure 9e shows the frequency dependence of the orientational order parameter of the colloidal crystals. The perfectly oriented single colloidal crystals are obtained in the low frequency range (400–800 Hz, low driving force regime). When the frequency increases to the high frequency range (1000–2000 Hz, high driving force regime), the degree of perfection gradually decreases.[31,33,35,37] For 1.8 μm PS particles, the interparticle separation r_{eq} among the assembly decreases with increasing frequency from 400 to 1000 Hz, and then reaches its minimum in the frequency range of 1000–2000 Hz, as shown in Figure 9e. This suggests that the attractive forces among the particles become more dominant with increasing frequency, and are much stronger than the repulsive ones in the frequency range of 1000–2000 Hz. In the high frequency range, the homogenous nuclei are very tightly assembled. Hence, the conformations and orientations of the homogenous nuclei are difficult to be rearranged by the attractions from the template when they approach the template. Therefore, the degree of perfection of the colloidal crystals decreases in the frequency range of 1000–2000 Hz. On the other hand, the nucleation rate, in the bulk fluid phase is large because of the increased attractive forces in the high frequency range (Figure 9e). Due to the increase in the homogenous nucleation rate, the entropy effect and the transport will result in a certain degree of randomness.[80] This will lead to a reduction of interfacial correlation between the template and the incoming growth units, thus, a decrease in the degree of perfection of the colloidal crystals and the mismatch with the template, which can be considered as the verification of the supersaturation-driven interfacial structural mismatch effect.

Recently, the effect of supersaturation-driven interfacial structural mismatch has been found to play a very important part in the pattern formation, crystallite network formation, supramolecules soft materials formation.[27,48–50]

3.5.3. Surface Roughening and Step Kinetics

The roughening transition is a type of phase transition which takes place on the crystal surface at the roughening temperature T_r: This phase transition can be generally characterized by the step free energy (per structural unit) $\gamma \sim kT$. Below the

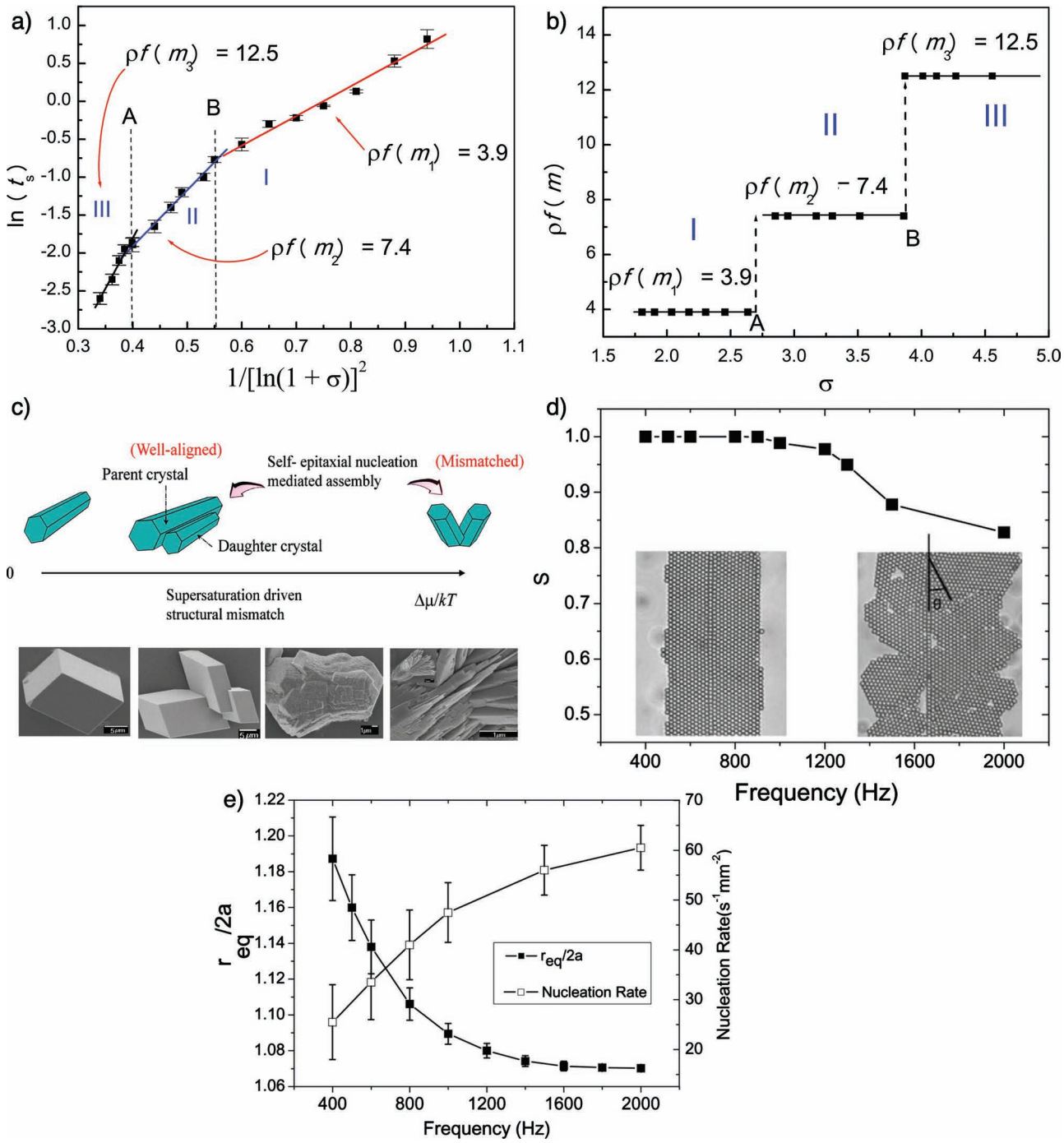

Figure 9. a) The plot of ln t_s vs $1/[\ln(1+\sigma)]^2$ for $CaCO_3$ (calcite) nucleation. Within the range of supersaturations where experiments were carried out, three straight lines with different slopes intercept one another, dividing the space into three regimes. b) Supersaturation driven interfacial structural mismatch: with the increase of the supersaturation, the interfacial correlation factor *f(m)* will increase abruptly at a certain supersaturation, such as A, B,…, corresponding to the transition from an ordered and structurally matched to a less ordered and structurally mismatched biomineral/substrate interface. c) Supersaturation-driven interfacial structure mismatch nucleation: The structural match between the daughter crystals and the parent crystal will become poor as supersaturation increases. d) and e): Colloidal crystallization modeling of supersaturation-driven interfacial structure mismatch nucleation: d) Frequency dependence of the orientational order parameter *S* under an AEF. Also shown are the optical images of a perfectly oriented colloidal crystal (left inset, $S = 1$) and a roughly oriented colloidal crystal (right inset, $S = 0.83$), assembled at 800 Hz and 2000 Hz for 10 min, respectively. e) Variation of $r_{eq}/2\,a$ and nucleation rate in the bulk fluid phase with frequency for 1.8 μm PS particles. Panels (a,b) reproduced with permission.[79] Copyright 2003, American Chemical Society. Panels (d,e) reproduced with permission.[41] Copyright 2008, American Institute of Physics.

roughening transition temperature T_r, due to the existence of γkT (or two-dimensional nucleation barrier), the crystal surface will keep its overall flatness corresponding to the orientation (*hkl*).[54] When the growth of a crystal surface occurs under its roughening temperature, there will be a non-zero free energy, the so-called step free energy associated with the creation of a

step of unit length at the surface.[81] Such a crystal face has the atomically smooth surface. Due to the step free energy, the creation of a new layer on the existing layer of the crystal surface requires overcoming a free energy barrier, so-called two-dimensional nucleation barrier. Normally, the growth of crystals will be governed by the dislocation-related growth mechanism (ie. the screw dislocation mechanism.[54] If the crystals are free of dislocations, their growth will be governed by the mechanism of 2D nucleation[81a,b,c] and the growth rate R_g is largely determined by the 2D nucleation rate. Above T_r, the step free energy vanishes and steps or kinks exist on the surface permanently even without screw dislocations. It follows that the surface will become rough microscopically and its crystallographic orientation is lost.

The roughening transition has been investigated in great deal by computer simulations,[54,81a,d] based on the so-called solid-on-solid (SOS) interfacial model.[54,81a] This model is a generalization of the Ising model, where the crystal surface is considered as a collection of interacting columns. The Hamiltonian of this model system can be taken as

$$H = \gamma_E \sum_{\langle ij \rangle} |h_i - h_j|^2 \quad (41)$$

(Here γ_E is the step energy per unit length, and the column heights, h_i, are restricted to integer values.) This most simple model is well understood since the relationship with the planar XY model has been established.[54,81d,e] It follows that the roughening transition described in this model is of the Kosterlitz-Thouless (KT) type[81d,e] (or a phase transition of infinite order), which is characterized by the step free energy γ which vanishes continuously:

$$\gamma \sim \exp\left[-\alpha (T - T_r)^{-1/2}\right] \text{ as } T \to T_r (T < T_r) \quad (42)$$

It was found experimentally that the roughening transition can be of infinite order or first order.[54,81] Although the computer simulations have acquired the images at the single particle scale, we have never acquired any experimental results concerning the process at the single particle level before. In addition, previously the theoretical analyses and computer simulations only predict that the roughening transition at the two layer solid-fluid interface can only be a second order phase transition.

In this regard, a two-dimensional assembly of charged colloidal particles induced by an alternating electric field in real space was adopted to model the roughening transition at the crystal surface. This is a typical example of the two layer solid-fluid interface.[36] To examine the roughening transition at the single particle scale, a two-dimensional assembly of charged colloidal particles induced by an alternating electric field was studied in real space by means of digital video microscopy. In such a system, the 2D colloidal crystals can be regarded as the top layer of "atoms" or "molecules" on the crystal surfaces. It follows that phase transitions occur from a highly ordered colloidal monolayer to an isotropic suspension by changing the field strength or frequency (in the appropriate range).[36] In particular, it is found that the strength-dependent phase transition is an infinite-order phase transition, in contrast to the frequency-dependent phase transition, which is a second-order phase transition.[36] It should be pointed out that the fact that both the infinite-order and the second order surface roughening transition at the two layer solid-fluid interface has never been recognized before either from theoretical analyses and computer simulations.

Apart from the surface roughening, the electrically controlled 2D colloidal crystallization can be applied to the many important processes, i.e., step, and defect formation and migration kinetics.[24,26,32,38,39]

4. Fabrication of Photonic Crystals based on Colloidal Crystals

Apart from the advancing of our knowledge in crystallization, colloidal crystallization has a wide range of applications in different areas. Among these, fabricating photonic crystals is one of the most important applications. The periodic modulation of the refractive index in a dielectric material creates a forbidden gap in the photonic band structure which is not allowed the existence of optical modes within a specific range of frequencies. Such photonic band-gap materials, known as photonic crystals, are attractive optical materials for controlling and manipulating light. In the last decades, a number of methods have been developed to fabricate photonic crystals at various length scales, including layer-by-layer stacking techniques using microfabrication tools,[82–84] electrochemical etching,[85,86] laser-beam-scanning chemical vapor deposition,[87] and holographic lithography.[88,89] Colloidal crystal, the periodic modulation of the dielectric constant is realized by self-assembling monodisperse colloidal objects such as silica (SiO_2) or polystyrene (PS) microspheres into ordered arrays, turns out to be an effective approach to photonic crystal preparation.[90–93] The resulting photonic properties are determined by the symmetry and lattice constant of the crystal and the refractive index contrast between the colloids and the surrounding medium. The sizes of colloids are typically in the range of 100 nm to several μm. The self-assembly and fabrication of two- or three-dimensional (2D/3D) colloidal crystals have attracted broad interest because their wide applications in photonic crystals,[4,94–96] chemical and biochemical sensors,[97,98] optoelectronic devices[99,100] and templates for colloidal nanolithography.[101]

4.1. Fabrication of 2D Colloidal Crystals and Templating

The commonly used methods to fabricate self-assembled monodispersed colloidal particles into ordered 2D arrays are based on the lateral capillary interaction, which originates from the deformation of the liquid surface.[102–105] The colloidal particles are typically assembled at the air–liquid interface or in a thin liquid layer supported on a flat, clean and chemically homogeneous solid substrate in terms of the surface pressure and convection.[106–111] Another method to create 2D arrays is electrophoretic deposition, which applies a strong electric field to assemble colloidal dispersions confined between two parallel solid electrodes as outlined above.[35–45]

To achieve practical applications, two major obstacles need to be overcome in fabricating 2D colloidal crystal. Firstly, many applications for colloidal crystals require samples which are free from defects over large length scales. However, most self-assembly systems suffer from disorders resulting from homogeneous nucleation and uncontrollable crystal growth. Secondly, the introduction of well-defined artificial defects within colloidal crystals is another prerequisite for some practical applications.[112] Linear defects, for instance, could be used as photonic waveguides and point defects as microcavities.[99] However, this cannot be achieved through conventional self-assembly methods alone, as the intentionally added defects will substantially frustrate the crystal growth and locally induce disordering in colloidal crystals.[113] Experimentally, a key challenging of controlling colloidal crystals is lack of reliable methods to control colloidal crystallization of large and perfect single crystals with predefined orientations, artificial defects, and patterns over fast time scales. Obviously, the electrically controlled 2D colloidal crystallization is one of the most promising technologies to acquire large and perfect 2D crystals based on the principles outlined in Section 3.5.1.

4.2. Fabrication of 3D Photonic Crystals

The technologies adopted to fabricate the 2D colloidal crystals can be extended to fabricate 3D colloidal crystals with some modifications. Several other methods have also been widely employed to assemble highly ordered 3D crystals with large domain size, including sedimentation, repulsive electrostatic interactions, and physical confinement. Among these, sedimentation in a gravitational field seems to be the simplest approach for building 3D colloidal crystals.[114] A number of parameters must be carefully controlled to grow colloidal crystals of high quality. These parameters include the size, uniformity, and density of the colloids, as well as the rate of sedimentation. The main disadvantages of this method are the poor control over the structure and the thickness of the crystalline arrays, the long preparation time, and the polycrystalline nature of the products. Highly charged colloids particles suspended in a solution can spontaneously self-organize into ordered structures, driven by the minimization of electrostatic repulsive interactions.[115–119] The colloidal crystals prepared using this method are typically non-close-packed, because the repulsive electrostatic interactions keep the particles away from each other. This method has very strict requirements regarding the experimental conditions such as the surface charge density, the colloidal concentration, and the ionic strength. By leaving the colloidal suspension to a physical confinement, it would self-assemble into long-range-ordered crystalline structures.[120–122] Colloidal crystals with domain sizes of square centimeters could be fabricated by using a specially designed packing cell.[123–125] This method is relatively fast, and it also provides tight control over the structures and the thickness of the 3D colloidal crystals. In Section 5.1, we will discuss the applications of 2D/3D colloidal crystals in structural color mimicking.

5. Mimicking of Structural Color

Structural color, caused by the interaction of light with the nanoscale periodic structures of certain materials,[126] has attracted extensive attentions for decades due to its wide applications in photonic crystals, cosmetics, and display technology.[127,128] In nature, the colorful feathers of many birds (ie. peacock), the wings of various butterflies and the shells of beetle are the excellent examples of structural colors.[129–133] It follows that the two dimensional photonic-crystals in the cortex of different colored barbules, are responsible for the coloration of peacock feather,[131,132] while the multi-layer structures of wing scales produce the structural coloration of some breeds of butterflies.[133] Compared with other coloring schemes, structural color is longer lasting, brighter and more deeply saturated.

5.1. Mimicking Structural Color Using Colloidal Crystals

During the last two decades, much effort has been devoted to mimicking natural structural color. However, to obtain the dedicated structures with the structural color as seen in animal kingdom (**Figure 10**a) remains to be a big challenge. One way to acquire structural color was to adopt the nature structural color materials as templates to replicate the nanostructures so as to

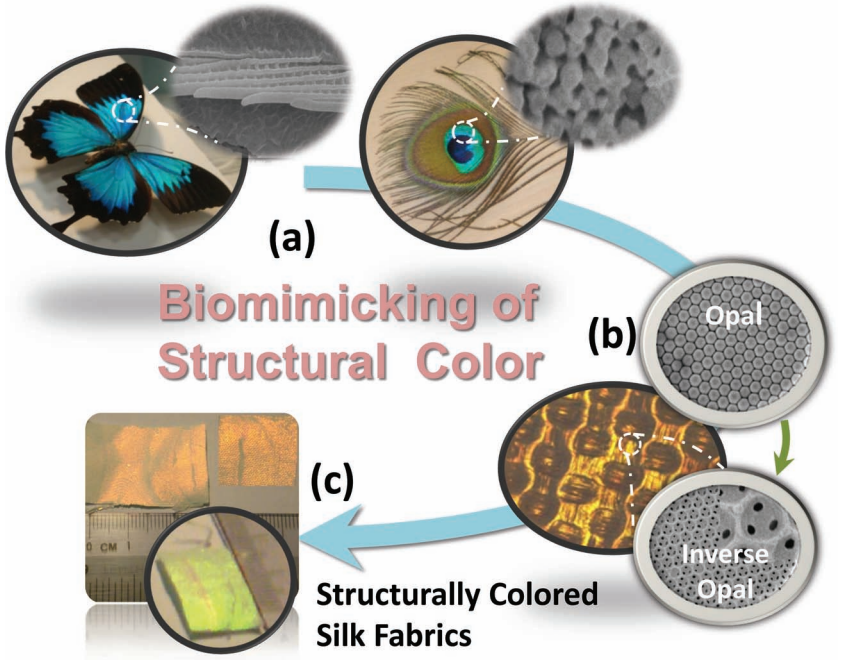

Figure 10. Biomimicking of structural colors on silk fabrics. a) The structure colors of butterfly (*Papilio Ulyssess* butterfly) and peacock feather. b) Fabrication of opal and inverse opal on silk fabrics.[143] c) Structurally colored silk fabrics.

obtain the optical properties. Wang et al. examined the fine structure of the wing scale of a *Morpho Peleides* butterfly and replicated the entire configuration by a uniform Al_2O_3 coating through a low-temperature atomic layer deposition (ALD) process.[134] An inverted structure was achieved by removing the butterfly wing template at high temperature, forming a polycrystalline Al_2O_3 shell structure with precisely controlled thickness. Other than the copy of the morphology of the structure, the optical property, such as the existence of PBG, was also inherited by the alumina replica. Other replicating methods have also been employed to replicate the structures of natural photonic materials, including conformal-evaporated-film-by-rotation technique, soft lithography technique, etc.[135,136]

3D colloidal crystals with a photonic band gap (PBG) lying in the visible range are another option for mimicking natural structural color.[137–143] Inspired by natural photonic crystals (Figure 10), researchers have fabricated colloidal crystals with tunable structural colors.[137–143] One of the most commonly used techniques to fabricate colloidal crystals is the evaporation-induced self assemble method, which enables the rapid production of highly ordered 3D colloidal crystals with face-center cubic structure. In connection with this technology, the wettability can be adjusted by the intrinsic roughness of colloidal crystals in combination with the tunable chemical composition of latex surfaces while the band gaps can be tuned by changing the size of the colloidal spheres.

To create structural colors on fabrics is a challenging task, but remains to be extremely important in practice. As color fading caused by leaching or oxidation/bleaching is a key problem in fabric care, producing with vivid and durable structural colors on fabrics by fabricating the 3D colloidal crystals onto the surface of fabrics will revolutionize textile and fashion industries.[143] If the physical structure of photonic crystals on the fabrics are strong enough, the colors will last forever. Recently, a combined surface treatment technology[143] allows us to create opal and/or inverse opal structures on silk fabrics (cf Figure 10). In producing structural colors on silk fabrics, polystyrene spheres with different diameters were assembled on the surface of silk fabrics. Silk fibroin was dispersed on the colloidal crystals as binding materials (Figure 10b). Thus, silk fabrics with different reflection peaks ranging from Ultraviolet to Near-Infrared can be obtained. It follows that the colors (the reflected wave lengths) can be created by tuning the lattice constant of the inverse opal, a, according to $\lambda = va$ (v: a function of the refractive index of the material).[137–143]

Moreover, by controlling the band gaps of the photonic crystals, multi functional silk fabrics may also be invented. For instance, we can acquire the UV protective clothing by creating photonic crystals or inverse capable of reflecting UV light. Similarly, the thermal insulating performance due to a reflection peak in the IR range will create cooling textiles in a hot summer. On the other hand, it will preserve to some extent our body heat in a cold winter if the IR reflecting structure is generated in the inner layer of textiles.

5.2. Structural Color Mixing

Although great accomplishment has been made, the structural color produced by the animal kingdom are much richer and more effective than what we can produce so far. Furthermore, it is especially difficult to mimic some unique optical properties of natural structural color, such as polarization, colors mixing etc. In the following, we will describe the structural color mixing and polarization effect produced by *Papilio* butterfly and a method utilizing a combined colloidal crystal and deposition technique to mimic these effects.

Apart from the iridescent visibility, naturl structural color produced by some animals also gives rise to additional unique optical properties and benefits. For instance, the brown barbules in male peacock tail feathers adopt mixed structural coloration.[132] Some breeds of *Papilio* butterflies reveal double reflection effect.[145,146]

The colors mixing mentioned above can be created by in different manners in nature.[151] **Figure 11**a depicts the double reflection and iridescent visibility created by the blue wing scales of *Papilio Ullysess*. The surface of its wings is composed of millions of scales. The scales of *P. Ulysess* are of a size around 150 μm × 90 μm, and consist of a fairly regular array of concavities. *P. Ulysess* exhibits a blue color under sunlight (Figure 11a(i)). When illuminated and observed at normal incident light, the concavities in *P. Ulysess* appear to be green (Figure 11a(ii)). However, upon crossing an input linear polarizer with an exit analyzer, the green reflected light in *P. Ulysess* almost disappear while the deep purple (near-UV) color reflected by ridges in *P. Ulysess* reflect back (Figure 11a(iii) & (iv)). This implies that the purple reflected light is not altered by the polarizers. By further characterization of the microstructures of the wing scales, it was found that the profile of the concavities was almost flat, the ridges run through the full length of the scales with a periodicity of 4-5 μm (Figure 11a(iv)). The configuration of the ridges is a 2D array of 70 nm × 100 nm rectangular air squares surrounded by organic cuticle layers (the main and sub-ribs) with a periodicity of ~140 nm ($D_1 + d_1$) along its length direction and ~160 nm ($D_2 + d_2$) along the main ribs. This long-range ordered structure with a very small periodicity can be considered to be a 2D photonic crystal slab tilt about 30° with respect to the surface of the scales. As shown in Figure 11a(v), the transverse cross section of the wing scales consists of 21 alternative cuticle and air layers, which share almost the same thickness (~95 nm). The multi-layer structure of the concavities (Figure 11a(iii) produce the green reflection light and give rise to a main reflection peak at ~550 nm for normal incident light. The 2D photonic crystal slab of the ridges which tilt ~30° to the surface of scales, interacting with the normal incident light at 60° and producing a small reflection locates at ~380 nm. These two reflection peaks mixed to the blue color perceived by human eyes.

The bright green colored wings of *P. Blumei* (Figure 11b, another breed of *Papilio* butterfly) result from a juxtaposition of blue and yellow-green light reflected from different microscopic regions on the wing scales. Optical microscopy reveals that these regions are the centers (yellow) (Figure 11b(ii)) and the edges (blue) of concavities (Figure 11b(iii)). Unlike *P. Ulysess*, the concavities of *P. Blumei* are cap shaped, of 4–6 μm in diameter (Figure 11b(vi)). The profile is much deeper than *P. Ulysess*. The inclined sides of each concavity tilt ~45° with respect to the horizontal surface, and the opposites of each concavity are perpendicular to each other. The ridges run through

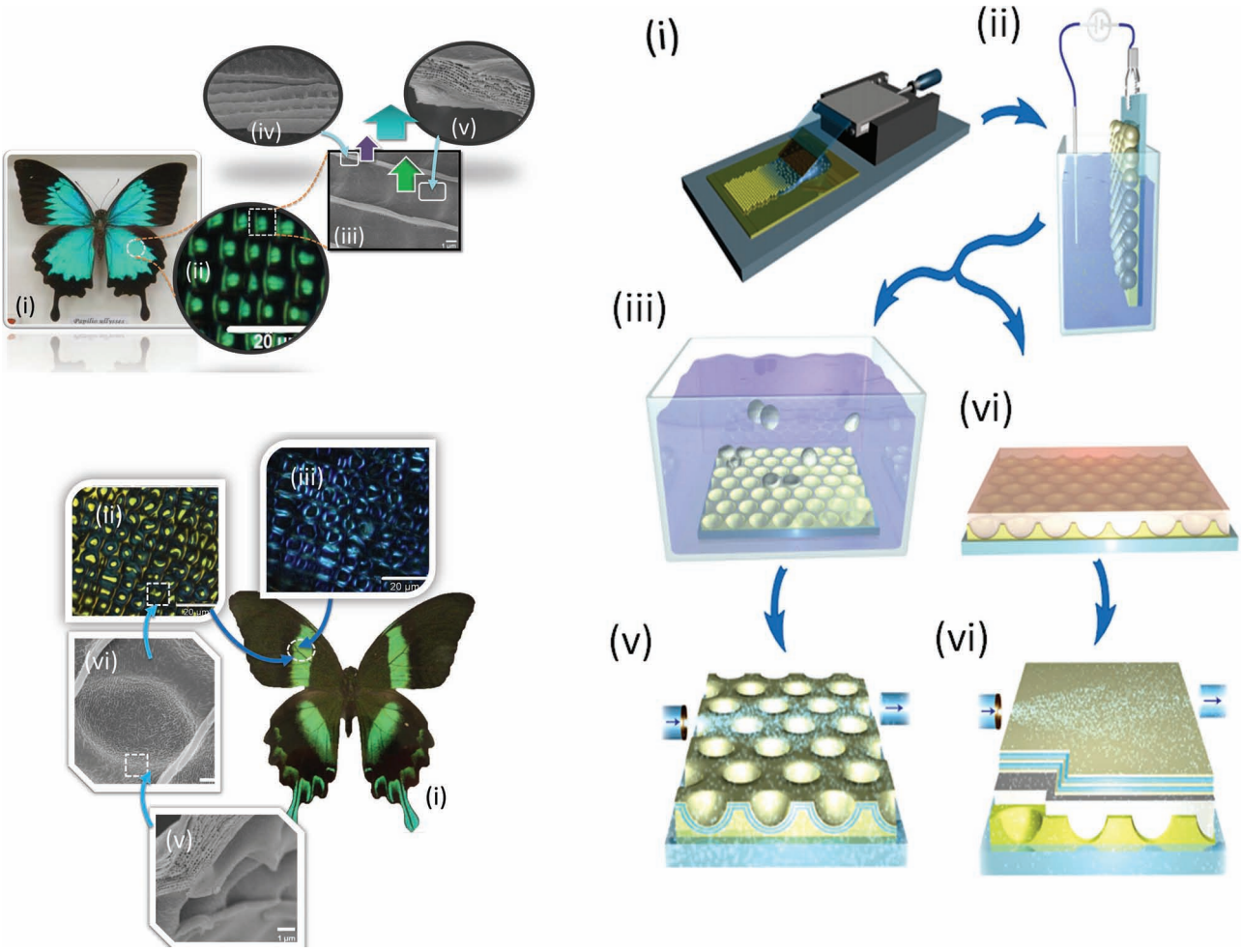

Figure 11. a) Nature photonic structure, *Papilio Ulyssess* butterfly. (i) The bright blue wings of *P. Ulysess* butterfly resulted from the mixed colors from different regions of the scales. (ii) and (iii) Optical (scale bar: 20 μm) and scanning electron (scale bar: 1 μm) microscapy images showing that the surface of a wing scale of a fairly regular array of concavities and ridges (iv). The concavities reflect green color light. (iv) UV light reflected from the ridges. (v) The transverse cross section of concavities of 21 alternative cuticle and air layers with thickness of ~95 nm, which reflect green light consistently.[151] Refs. [151]. b) Natural photonic structure: *Papilio Blumei* butterfly. (i) The bright green wings of the *P. blumei* butterfly resulted from the mixing of the different colors of light from different regions of the wing scales. (ii) and (iii), Optical microscopy images (scale bar: 20 μm) showing that the concavities reflect yellow and blue colors under normal incident light. (vi) Scanning electron microscopy image showing that the surface of a wing scale is covered with concavities (diameter ≈ 5–10 μm); (v) The transverse cross section of concavities consists of 21 alternative cuticle and air layers with thickness of ~120 nm. (From[151]) (c) Sample fabrication. (i) Deposition of polystyrene colloids on a gold-coated silicon substrate. (ii) Growth of platinum or gold in the interstices of the colloidal array by electro-plating. The metal deposition is terminated when the thickness of the deposited film equals the microsphere radius. (iii) Removal of the polystyrene spheres from the substrate by ultrasonication in acetone. (v) Sputtering of a thin carbon film and ALD of a stack of 11 alternating TiO_2 and Al_2O_3 layers (arrows indicate the precursor gas flow). In a second route, the colloids are molten to cover the cavities with a homogeneous film (vi) which is covered by a TiO_2–Al_2O_3 multilayer.[144] Panel (c) reproduced with permission.[144] Copyright 2010, Nature Publishing Group.

the full length of each scale with a periodicity of 7–8 μm. The transverse cross section of the concavities also consists of 21 alternative cuticle and air layers with a thickness around 110 nm (Figure 11b(v)). For the normal incident light, theoretical calculation predicts that the reflection peak resulted from the flat portions locates at 600 nm, in agreement with the yellow color observed under optical microscopy; while the light incident on the edges of concavities with an angle ~45°, producing a reflection peak at ~450 nm, in accordance with the blue color observed under optical microscope. The light incident on one side of the concavity, reflected from one 45° side, travels across the concavity to the opposite orthogonal side, and then reflects backward in parallel to the original incident direction. Through this double reflection process, the blue reflected light undergoes a polarization conversion. As a result, it survives upon the crossed polarizers. These two colors mix up the green coloration caught by human eyes. It follows that the two breeds of butterfly take advantage of the colors mixing strategy. The blue color of *P. Ulysess* is mixed by the green and deep purple colors reflected by concavities and ridges respectively. The green color seen from *P. Blumei* is a mixture of yellow and blue colours reflected by the flat portions and inclined sides of concavities. We notice

that many studies show that the eyes of the butterflies have a duplicated gene, allowing them to see ultraviolet colors and distinguish the spectral properties and spatial distribution of the visual colors.[148] And also, they are sensitive to the polarized light. Therefore, the knowledge on the structural origination of the two reflection peaks and polarization property of butterfly wings would have broad biological implications.[147,149] Furthermore, with the understanding of the correlation between the optical properties and the corresponding structures, researchers could be able to find a way to mimic natural structural colors with designated properties. Evidently, the ability to mimic the structural colour with its spectacular function will broaden the biomimicry field in the design of structural colour materials targeted for ultra and smart performance.

M. Kolle et al. adopted the combined techniques of colloidal crystal self-assembly, sputtering and atomic layer deposition to fabricate photonic structures that mimic the colors mixing and polarization effect found on the colored wing scales of *Papilio Blumei*.[144] They demonstrated the replication of the periodically shaped multilayer structure of the *Papilio* butterfly scale in five steps (Figure 11c). Polystyrene colloids with a diameter of 5 μm were assembled on a gold-coated silicon substrate to create regularly arranged concavities. A layer of platinum or gold with thickness ~2.5 μm was then electrochemically grown into the interstitial space between the colloids, creating a negative replica.[152–154] Ultrasonication of the sample in dimethylformamide or acetone removed the colloids, resulting in a template of hexagonally arranged metal concavities. A ~20-nm-thick carbon film was sputtered onto the gold surface. Finally, a conformal multilayer of thin quarter-wave titania and alumina films was grown by ALD.[155] The carbon layer between the gold (or platinum) and the multilayer stack adsorbs light passing through the multilayer stack, reducing specular reflections and unwanted destructive interferences that would otherwise severely limit the optical performance.

During the fabrication process, the diameter and height of the concavities for the artificial mimic were well controlled by the size of colloidal spheres and thickness of platinum or gold layer. The number of the alternating titania and alumina layers, as well as their thicknesses could be carefully controlled during the ALD process. By choosing proper thicknesses of the titania and alumina layers, the stop-band centre wavelength for the artificial multi-layer structure could locate ~550 nm, matching the reflectance band of the natural *P.Blumei* structure closely. Due to the concave structure, the center of the concavities exhibit yellow-green reflection (~550 nm), while the reflection light from the four segments of the concavities blue-shifts to blue color. The observation of the artificial mimic between crossed polarizers leads to a similar effect as described for the *P.Blumei* structure. Only light incident onto four segments of the concavity edges is detected. The local surface normal of ~45° gives rise to a double reflection at the opposing cavity walls, causing a polarization rotation. The artificial mimic therefore displays the same optical characteristics as the natural *P. blumei* wing scale structure.

Nevertheless, this approach described above needs to fabricate complex nanostructures, wherein the two reflections come from different parts of the structure. This technique is costly and difficult to obtain different properties by tuning the structure. In this regard, the key challenges in future work to biomimic natural structural color turn out to be how to design and fabricate photonic crystals with the unique optical properties of natural structural color through a simple process. One promising way is to construct photonic crystals with two photonic band gaps to get the desired double reflection. On the other hand, the growing demand for optical interfaces and sensors for biomedical applications is motivating research towards realizing biocompatible photonic components that offer a seamless interface between the optical and biological worlds. Therefore, another key issue in this field is how to mimic the double reflection effect using biocompatible and biodegradable materials.

We notice that the double reflection has its biological function. For instance, there are three major photoreceptors in the compound eye of *Heliconius erato* with spectral sensitivity peaks at 370 nm, 470 nm, and 560–570 nm, allowing the detection of ultraviolet colors, and the distinguish of the spectral properties of visible light.[147] It follows that the double reflection of butterfly wings giving rise to both visible and UV reflections may serve for communication and mating signals in butterfly kingdom.[147–149] Thus, investigating the correlation between the optical properties and the structures may help to explain the innate behaviors of the butterfly kingdom. Investigating the colouration mechanisms of these optical properties and the corresponding structures also has crucial implications for biomimicry, including colour-stimulus synthesis, display technologies, various polarization applications.[112,150]

6. Conclusions

As can be seen from the results presented in this paper, almost all fundamental aspects of crystallization can be examined in terms of the AEF controlled 2D colloidal crystallization system. The studies based on such a model system have given rise to some new knowledge on crystallization. For instance, although it has been confirmed that the classical nucleation theories can be applied to describe the nucleation dynamics, the initial stage of nucleation may not be exactly the same as we expected. Unlike the assumption that both the embryos and the bulk crystals share the same structure, the structures of the embryos are supersaturation dependent. Such a deviation would be beneficial in lowering the nucleation barrier, and then facilitate the nucleation kinetics at low supersaturations. From the point of view of solid-fluid interface, the above "experimental modeling" can also provide some unique and extremely relevant information, which is capable of updating our knowledge in crystallization in general. Utilizing such a model system, we can verify that a cluster of growth unites can be incorporated into the steps without causing any defect. In this process, the self orientation of the clusters plays an important role. Similarly, we can also visualize the so-called self perfection process, where the defect lines are repelled from the crystal-substrate interface. Notice that the effect of supersaturation driven structure mismatch has been put forward, but never been confirmed directly before. The templated 2D colloidal nucleation provides the first observation of this effect. Such an experimental modeling system has been successfully applied to examine many other

crystallization processes, i.e., multistep crystallization, roughening transition, adatomic step integration, defects generation and migration kinetics, etc., which have never been examined quantitatively before at the single particle level. Note that the key advantage of the experimental modeling system is the combination of the visualization and the quantitative treatment, which advance our knowledge to a new phase. For instance, previously the theoretical analyses and computer simulations only predict that the infinite-order surface roughening transition can only occur in the solid-on-solid multi layer mode while one can only have a second-order phase transition at the two layer solid-fluid interface. Nevertheless, the modeling based on the 2D colloidal crystallization indicated that we can have both the infinite-order and the second order surface roughening transition at the two layer solid-fluid interface if we choose different parameter sets. This allows us to check the theories directly. As the colloidal crystallization system displays the phase behaviors similar to normal crystalline materials, and the crystallization condition can be controlled easily and precisely, it can be foreseen that this approach will become a powerful tool to study the science and technology of crystallization. In the area of application, apart from the fabrication of photonic devices, sensors, and tunable lasers etc., colloidal crystallization has been now applied to mimic the structure colors and double reflection on silk fabrics, which will exert a significant impact on textile, personal care and fashion industries.

Acknowledgements

The authors acknowledge the support from Singapore ARC funding (Project No. T13-0602-P10).

Received: September 25, 2011
Published online: February 10, 2012

[1] C. S. Hirtzel, R. Rajagopalan, *Colloidal Phenomena: Advanced Topics*, Noyes, Park Ridge, NJ **1985**, 15.
[2] D. F. Evans, H. Wenneerstrom, *The Colloidal Domain: Where Physics, Chemistry, Biology, and Technology Meet*, Wiley-VCH, Weinheim **1994**, 187.
[3] J. S. Bradley, in *Clusters and Colloids*, (Ed: G. Schmid) Wiley-VCH, Weinheim **1994**, 459.
[4] Y. A. Vlasov, X.-Z. Bo, J. C. Sturm, D. J. Norris, *Nature* **2001**, *414*, 289.
[5] W. Cheng, J. Wang, U. Jonas, G. Fytas, N. Stefanou, *Nat. Mater.* **2006**, *5*, 830.
[6] J. Holtz, S. A. Asher, *Nature* **1997**, *389*, 829.
[7] J. R. Lawrence, Y. Ying, P. Jiang, S. H. Foulger, *Adv. Mater.* **2006**, *18*, 300.
[8] W. Ostwald, *Z. Phys. Chem.* **1897**, *22*, 289.
[9] P. R. ten Wolde, D. Frenkel, *Phys. Chem. Chem. Phys.* **1999**, *1*, 2191.
[10] W. Poon, *Science* **2004**, *304*, 830.
[11] D. Frenkel, *Science* **2002**, *296*, 65.
[12] V. J. Anderson, H. N. W. Lekkerkerker, *Nature* **2002**, *416*, 811.
[13] F. Nadal, F. Argoul, P. Hanusse, B. Pouligny, A. Ajdari, *Phys. Rev. E* **2002**, *65*, 061409.
[14] M. R. Philpott, in *Nanoscale structure and assembly at solid-fluid interfaces*, (Eds: X. Y. Liu, James J. De Yoreo) Springer, London **2004**, Vol. *I*, ch 1.
[15] K. Q. Zhang, X. Y. Liu, *Nature* **2004**, *429*, 739.
[16] D. G. Grier, C. A. Murray, *J. Chem. Phys.* **1994**, *100*, 9088.
[17] A. van Blaaderen, P. Wiltzius, *Science* **1995**, *270*, 1177.
[18] W. K. Kegel, A. van Blaaderen, *Science* **2000**, *287*, 290.
[19] J. W. Gibbs, *Collected Works. Vol. I: Thermodynamics*, Longmans and Green, New York **1928**.
[20] M. Votmer, A. Weber, *Z. Phys. Chem.* **1926**, *119*, 277.
[21] L. Farkas, *Z. Phys. Chem.* **1927**, *125*, 236.
[22] R. Kaischew, I. Stranski, *Z. Phys. Chem B* **1934**, *26*, 317.
[23] R. Becker, W. Doering, *Ann. Phys.* **1935**, *24*, 719.
[24] J. B. Zeldovich, *Acta Physicochim. URSS* **1943**, *18*, 1.
[25] J. P. Hirth, G. M. Pound, *Condensation and Evaporation*, Pergamon, Oxford **1963**.
[26] A. E. Nielsen, *Kinetics of Precipitation*, Pergamon, Oxford **1964**.
[27] X. Y. Liu, in *Nanoscale structure and assembly at solid-fluid interfaces*, (Eds: X. Y. Liu, James J. De Yoreo) Springer, London **2004**, *I*, 109.
[28] P. G. Vekilov, O. Galkin, in *Nanoscale structure and assembly at solid-fluid interfaces*, (Eds: X. Y. Liu, James J. De Yoreo) Springer, London **2004**, *II*, Ch 4.
[29] U. Gasser, E. R. Weeks, A. Schofield, P. N. Pusey, D. A. Weitz, *Science* **2001**, *292*, 258.
[30] D. H. Everett, *Basic Principles of Colloidal Science*, The Royal Society of Chemistry, Cambridge **1988**.
[31] Y. Liu, J. Narayanan, X. Y. Liu, *J. Chem. Phys.* **2006**, *124*, 124906.
[32] T. H. Zhang, X. Y. Liu, *Appl. Phys. Lett.* **2006**, *89*, 261914.
[33] Y. Liu, X. Y. Liu, J. Narayanan, *J. Phys. Chem. C* **2007**, *111*, 995.
[34] T. H. Zhang, X. Y. Liu, *J. Phys. Chem. C* **2007**, *111*, 1342.
[35] K. Q. Zhang, X Y. Liu, *Appl. Phys. Lett.* **2007**, *90*, 111911.
[36] K. Q. Zhang, X. Y. Liu, *Phys. Rev. Lett.* **2006**, *96*, 105701.
[37] Y. Liu, R. G. Xie, X. Y. Liu, *Appl. Phys. Lett.* **2007**, *90*, 063105.
[38] T. H. Zhang, X. Y. Liu, *J. Am. Chem. Soc.* **2007**, *129*, 13520.
[39] T. H. Zhang, X. Y. Liu, *J. Phys. Chem. B* **2007**, *111*, 14001.
[40] R. G. Xie, X. Y. Liu, *Adv. Funct. Mater.* **2008**, *18*, 802.
[41] R. G. Xie, X. Y. Liu, *Appl. Phys. Lett.* **2008**, *92*, 083106.
[42] R. G. Xie, X. Y. Liu, *J. Am. Chem. Soc.* **2009**, *131*, 4976.
[43] T. H. Zhang, X. Y. Liu, *Angew. Chem. Int. Ed.* **2009**, *48*, 1308.
[44] K. Q. Zhang, X. Y. Liu, *J. Chem. Phys.* **2009**, *130*, 184901.
[45] K. Q. Zhang, X. Y. Liu, *Langmuir.* **2009**, *25*, 5432.
[46] M. Trau, D. A. Saville, I. A. Aksay, *Science* **1996**, *272*, 706; *Langmuir* **1997**, *13*, 6375.
[47] S. R. Yeh, M. Seul, B. I. Shraiman, *Nature* **1997**, *386*, 57.
[48] X. Y. Liu, in *Advances in Crystal Growth Research*, (Eds: K. Sato, K. Nakajima, Y. Furukawa) Elsevier, Amsterdam **2001**, p42–61.
[49] X. Y. Liu, in *Perspectives on Inorganic, Organic and Biological Crystal Growth: from Fundamentals to Applications*, (Eds: M. Skowronski, J. J. DeYoreo, C. A. Wang) American Institute of Physics, Park City, UT **2007**, p.439–465.
[50] a) J. L. Li, X. Y. Liu, *Adv. Funct. Mat.* **2010**, *20*, 3196–3216; b) X. Y. Liu, in Low Molecular Mass Gelators: Design, Self-Assembly, Function, *Topics in Current Chemistry*, (Ed: F. Frédéric), Springer, Berlin **2005**, Chapter 1, p.1–37.
[51] X. Y. Liu, *J. Chem. Phys.* **1999**, *111*, 1628; **2000**, *112*, 9949.
[52] R. Fowler, E. A. Giggenhein, *Statistical Thermodynamics*, Cambridge University, London **1960**.
[53] B. Mutaftschiev, Nucleation theory, in: *Handbook on Cryst. Growth*, (Ed: D. T. J. Hurle) North-Holland, Amsterdam **1993**, pp. 189–245.
[54] a) X. Y. Liu, in *Selected Topics on Crystal Growth: 14th International Summer School On Crystal Growth*, (Eds: Mu Wang, K. Tsukamoto, Di Wu), American Institute of Physics, New York **2010**, p.173–220; b) A. A. Chernov, *Modern Crystallography III—Crystal Growth*, Springer-Verlag, Berlin **1984**.
[55] X. Y. Liu, N. Du, *J. Biol. Chem.* **2004**, *279*, 6124.
[56] N. Du, X. Y. Liu, *Appl. Phys. Lett.* **2002**, *81*, 445.
[57] N. Du, X. Y. Liu, C. L. Hew, *J. Biol. Chem.* **2003**, *278*, 36000.

[58] J. Santana-Solano, D. T. Wu, D. W. M. Marr, *Langmuir* **2006**, *22*, 5932.
[59] A. C. Zettlemoyer, *Nucleation*, Dekker, New York **1969**.
[60] D. Kashchiev, *Cryst. Res. Technol.* **1984**, *19*, 1413.
[61] B. Lewis, J. C. Andersen, *Nucleation and Growth of Thin Films*, Academic, New York **1978**.
[62] J. F. Lutsko, G. Nicolis, *Phys. Rev. Lett.* **2006**, *96*, 046102.
[63] A. Navrotsky, *Proc. Natl. Acad. Sci.* USA **2004**, *101*, 12096.
[64] a) J. Zhang, X. Y. Liu, *J. Chem. Phys.* **2003**, *119*, 10972; b) J. Narayanan, X. Y. Liu, *Biophys. J.* **2003**, *84*, 523; c) P. S. Chow, X. Y. Liu, J. Zhang, R. B. H. Tan, *Appl. Phys. Lett.* **2002**, *81*, 1995.
[65] Y. W. Jia, X. Y. Liu, *Appl. Phy. Lett.* **2005**, *86*, 023903; Y. W. Jia, J. Narayanan, X. Y. Liu, Y. Liu, *Biophys. J.* **2005**, *89*, 4245.
[66] L. Wang, X. Y. Liu, *Biophys. J.* **2008**, *95*, 5931.
[67] P. R. ten Wolde, D. Frenkel, *Science* **1997**, *277*, 1975.
[68] C. Haas, J. Drenth, *J. Phys. Chem. B* **2000**, *104*, 368.
[69] E. Beniash, J. Aizenberg, L. Addadi, S. Weiner, *Proc. R. Soc. London Ser. B* **1997**, *264*, 461.
[70] L. Addadi, S. Raz, S. Weiner, *Adv. Mater.* **2003**, *15*, 959.
[71] H. H. Pan, X. Y. Liu, R. K. Tang, H. Y. Xu, *Chem. Commun.* **2010**, *46*, 7415.
[72] X. Chen, A. C. S. Samia, Y. Lou, C. Burda, *J. Am. Chem. Soc.* **2005**, *127*, 4372.
[73] D. Kashchiev, P. G. Vekilov, A. B. Kolomeisky, *J. Chem. Phys.* **1984**, *122*, 244706.
[74] Y. G. Kuznetsov, A. J. Malkin, A. McPherson, *J. Cryst. Growth* **2001**, *232*, 30.
[75] a) S. Auer, D. Frenkel, *Phys. Rev. Lett.* **2003**, *91*, 015703; b) X. Y. Liu, P. Bennema, J. P. van der Eerden, *Nature* **1992**, *356*, 778.
[76] P. G. Vekilov, *Crys. Growth Design* **2004**, *4*, 671.
[77] X. Y. Liu, P. van Hoof, P. Bennema, *Phys. Rev. Lett.* **1993**, *71*, 109.
[78] X. Y. Liu, E. S Boek, W. J. Briels, P. Bennema, *Nature* **1995**, *374*, 342.
[79] a) X. Y. Liu, S. W. Lim, *J. Am. Chem. Soc.* **2003**, *125*, 888; b) X. Y. Liu, *Appl. Phys. Lett.* **2001**, *79*, 3539.
[80] X. Y. Liu, *J. Chem. Phys.* **1999**, *111*, 1628.
[81] a) X. Y. Liu, *Phys. Rev. B* **1999**, *60*, 2810; b) X. Y. Liu, K. Maiwa, K. Tsukamoto, *J. Chem. Phys.* **1997**, *106*, 1870; c) X. Y. Liu, E. P. G. van den Berg, A. R. A. Zauner, P. Bennema, *J. Phys. Chem.* **2000**, *B104*, 11942. d) J. M. Kosterlitz, D. J. Thouless, *J. Phys. C* **1973**, *6*, 1181; e) X. Y. Liu, P. Bennema, J. P. van der Eerden, *Nature* **1992**, *356*, 778.
[82] S. Y. Lin, J. G. Fleming, D. L. Hetherington, B. K. Smith, R. Biswas, K. M. Ho, M. M. Sigalas, W. Zubrzycki, S. R. Kurtz, J. Bur, *Nature* **1998**, *394*, 251.
[83] J. G. Fleming, S.-Y. Lin, *Opt. Lett.* **1999**, *24*, 49.
[84] S. Noda, K. Tomoda, N. Yamamoto, A. Chutinan, *Science* **2000**, *289*, 604.
[85] A. Birner, R. B. Wehrspohn, U. M. Gsele, K. Busch, *Adv. Mater.* **2001**, *13*, 377.
[86] H. Masuda, M. Ohya, H. Asoh, M. Nakao, M. Nohtomi, T. Tamamura, *Jpn. J. Appl. Phys.* **1999**, *38*, L1403.
[87] M. C. Wanke, O. Lehmann, K. Mller, Q. Z. Wen, M. Stuke, *Science* **1997**, *275*, 1284.
[88] M. Campbell, D. N. Sharp, M. T. Harrison, R. G. Denning, A. J. Turberfield, *Nature* **2000**, *404*, 53.
[89] S. Shoji, S. Kawata, *Appl. Phys. Lett.* **2000**, *76*, 2668.
[90] Y. Xia, B. Gates, Y. Yin, Y. Lu, *Adv. Mater.* **2000**, *12*, 693.
[91] R. C. Schroden, M. Al-Daous, C. F. Blanford, A. Stein, *Chem. Mater.* **2002**, *14*, 3305.
[92] C. Lpez, *J. Opt. A* **2006**, *8*, R1.
[93] L. I. Halaoui, N. M. Abrams, T. E. Mallouk, *J. Phys. Chem. B* **2005**, *109*, 6334.
[94] J. E. G. J. Wijnhoven, W. L. Vos, *Science* **1998**, *281*, 802.
[95] D. J. Norris, Y. A. Vlasov, *Adv. Mater.* **2001**, *13*, 371.
[96] A. P. Hynninen, J. H. J. Thijssen, E. C. M. Vermolen, M. Dijkstra, A. van Blaaderen, *Nat. Mater.* **2007**, *6*, 202.
[97] J. H. Holtz, S. A. Asher, *Nature* **1997**, *389*, 829.
[98] O. D. E. Velev, W. Kaler, *Langmuir* **1999**, *15*, 3693.
[99] J. D. Joannopoulos, P. R. Villeneuve, S. Fan, *Nature* **1997**, *386*, 143.
[100] T. Yamasaki, T. Tsutsui, *Appl. Phys. Lett.* **1998**, *72*, 1957.
[101] S. M. Yang, S. G. Jang, D. G. Choi, S. Kim, H. K. Yu, *Small* **2006**, *2*, 458.
[102] C. A. Murray, D. H. VanWinkle, *Phys. Rev. Lett.* **1987**, *58*, 1200.
[103] W. R. Bowen, A. O. Sharif, *Nature* **1998**, *393*, 663.
[104] P. A. Kralchevsky, N. D. Denkov, Curr. *Opin. Colloid Interface Sci.* **2001**, *6*, 383.
[105] K. D. Danov, B. Pouligny, P. A. Kralchevsky, *Langmuir* **2001**, *17*, 6599.
[106] A. J. Hurd, D. W. Schaefer, *Phys. Rev. Lett.* **1985**, *54*, 1043.
[107] F. Burmeister, C. Schafle, T. Matthes, M. Bohmisch, J. Boneberg, P. Leiderer, *Langmuir* **1997**, *13*, 2983.
[108] H. H. Wickman, J. N. Korley, *Nature* **1998**, *393*, 445.
[109] V. N. Paunov, P. A. Kralchevsky, N. D. Denkov, K. Nagayama, *J. Colloid Interface Sci.* **1993**, *157*, 100.
[110] T. Miwa, K. Nagayama, *Langmuir* **1999**, *15*, 5257.
[111] P. A. Kralchevsky, K. Nagayama, *Langmuir* **1994**, *10*, 23.
[112] A. Arsenault, F. Fleischhaker, G. von Freymann, V. Kitaev, H. Miguez, A. Mihi, N. Tetreault, E. Vekris, I. Manners, S. Aitchison, D. Perovic, G. A. Ozin, *Adv. Mater.* **2006**, *18*, 2779.
[113] V. W. A. de Villeneuve, R. P. A. Dullens, D. G. A. L. Aarts, E. Groeneveld, J. H. Scherff, W. K. Kegel, H. N. W. Lekkerkerker, *Science* **2005**, *309*, 1231.
[114] A. K. Arora, B. V. R. Tata, *Ordering and Phase Transitions in Colloidal Systems*, VCH, Weinheim **1996**.
[115] P. Pieranski, *Contemp. Phys.* **1983**, *24*, 25.
[116] W. Van Negen, I. Shook, *Adv. Colloid Interface Sci.* **1984**, *21*, 119.
[117] S. A. Asher, P. L. Flaugh, G. Washinger, *Spectroscopy* **1986**, *1*, 26.
[118] P. L. Flaugh, S. E. O. Donnell, S. A. Asher, *Appl. Spectrosc.* **1984**, *38*, 847.
[119] R. J. Carlson, S. A. Asher, *Appl. Spectrosc.* **1984**, *38*, 297.
[120] D. H. VanWinkle, C. A. Murray, *Phys. Rev. A* **1986**, *34*, 562.
[121] P. Pieranski, L. Strzelecki, B. Pansu, *Phys. Rev. Lett.* **1983**, *50*, 900.
[122] S. Neser, C. Bechinger, P. Leiderer, T. Palberg, *Phys. Rev. Lett.* **1997**, *79*, 2348.
[123] S. H. Park, D. Qin, Y. Xia, *Adv. Mater.* **1998**, *10*, 1028.
[124] S. H. Park, Y. Xia, *Langmuir* **1999**, *15*, 266.
[125] B. Gates, D. Qin, Y. Xia, *Adv. Mater.* **1999**, *11*, 466.
[126] S Berthier, *Iridescence, The Physical Colours of Insets*, Springer, **2007**.
[127] S. S. Choi, S. M. Morris, W. T. S. Huck, H. J. Coles, *Adv. Mater.* **2010**, *22*, 53.
[128] A. C. Arsenault, D. P. Puzzo, I. Manners, G. A. Ozin, *Nat. Photonics* **2007**, *1*, 468.
[129] S. Kinoshita, S. Yoshioka, *ChemPhysChem* **2005**, *6*, 1442.
[130] S. Banerjee, Z. Dong, *Opt. Rev.* **2007**, *14*, 359.
[131] J. Zi, X. D. Yu, Y. Z. Li, X. H. Hu, C. Xu, X. J. Wang, X. H. Liu, R. T. Fu, *Proc. Natl. Acad. Sci. USA* **2003**, *100*, 12576.
[132] Y. Z. Li, Z. H. Lu, H. W. Yin, X. D. Yu, X. H. Liu, J. Zi, *Phys. Rev. E* **2005**, *72*. 010912
[133] S. Kinoshita, *Structural Colors in the Realm of Nature*. World Scientific Publishing Co., Singapore **2008**.
[134] Y. Chen, J. J. Gu, S. M. Zhu, T. X. Fan, D. Zhang, Q. X. Guo, *Appl. Phys. Lett.* **2009**, *94*. 053901.
[135] H. L. Ge, Y. L. Song, L. Jiang, D. B. Zhu, *Thin Solid Films* **2006**, *515*, 1539.
[136] J. X. Wang, Y. Q. Wen, H. L. Ge, Z. W. Sun, Y. M. Zheng, Y. L. Song, L. Jiang, *Macromol. Chem. Phys.* **2006**, *207*, 596.

[137] B. You, N. G. Wen, L. Shi, L. M. Wu, J. Zi, *J. Mater. Chem.* **2009**, *19*, 3594.
[138] J. X. Wang, Y. Q. Wen, J. P. Hu, Y. L. Song, L. Jiang, *Adv. Funct. Mater.* **2007**, *17*, 219.
[139] J. X. Wang, Y. Q. Wen, J. P. Hu, Y. L. Song, L. Jiang, *Macromol. Rapid Commun.* **2006**, *27*, 188.
[140] J. X. Wang, Y. Q. Wen, J. P. Hu, Y. L. Song, L. Jiang, *Acc. Chem. Res.* **2011**, *44*, 405.
[141] H. Fudouzi, Y. N. Xia, *Langmuir* **2003**, *19*, 9653.
[142] O. Sato, S. Kubo, Z. Z. Gu, *Acc. Chem. Res.* **2009**, *42*, 1.
[143] X. Y. Liu, Y. Y. Diao, *PCT/SG2011/000075* **2011**.
[144] M. Kolle, P. M. Salgard-Cunha, M. R. J. Scherer, F. M. Huang, P. Vukusic, S. Mahajan, J. J. Baumberg, U. Steiner, *Nat. Nanotechnol.* **2010**, *5*, 511.
[145] P. Vukusic, J. R. Sambles, C. R. Lawrence, *Nature* **2000**, *404*, 457.
[146] P. Vukusic, R. Sambles, C. Lawrence, G. Wakely, *Appl. Opt.* **2001**, *40*, 1116.
[147] A. D. Briscoe, S. M. Bybee, G. D. Bernard, F. R. Yuan, M. P. Sison-Mangus, R. D. Reed, A. D. Warren, J. Llorente-Bousquets, C. C. Chiao, *Proc. Natl. Acad. Sci. USA* **2010**, *107*, 3628.
[148] M. L. M. Lim, M. F. Land, D. Q. Li, *Science* **2007**, *315*, 481.
[149] Y. Takeuchi, K. Arikawa, M. Kinoshita, *J. Exp. Biol.* **2006**, *209*, 2873.
[150] T. Labhart, F. Baumann, G. D. Bernard, *Cell Tissue Res.* **2009**, *338*, 391.
[151] Y. Y. Diao, X. Y. Liu, *Opt. Express* **2011**, *19*, 9232.
[152] P. N. Bartlett, P. R. Birkin, M. A. Ghanem, *J. Chem. Soc. Chem. Commun.* **2000**, *17*, 1671.
[153] P. V. Braun, P. C. O. Wiltzius, *Colloid Interface Sci.* **2002**, *7*, 116.
[154] J. E. G. J. Wijnhoven, S. J. M. Zevenhuizen, M. Hendriks, D. Vanmaekelbergh, J. J. Kelly, W. L. Vos, *Adv. Mater.* **2000**, *12*, 888.
[155] R. L. Puurunen, *J. Appl. Phys.* **2005**, *97*, 121301.